Summer 2015

Design of High Temperature Evaporator for Spectroscopic Study of Equilibrated Vapor Phase Materials

Yarden Bosch

DESIGN OF HIGH TEMPERATURE EVAPORATOR FOR SPECTROSCOPIC STUDY OF EQUILIBRATED VAPOR PHASE MATERIALS

A Masters Thesis

Presented to

The Graduate College of

Missouri State University

In Partial Fulfillment

Of the Requirements for the Degree

Master of Science, Materials Science

By

Yarden Bosch

July 2015

DESIGN OF HIGH TEMPERATURE EVAPORATOR FOR SPECTROSCOPIC STUDY OF EQUILIBRATED VAPOR PHASE MATERIALS

Physics, Astronomy, & Materials Science

Missouri State University, July 2015

Master of Science

Yarden Bosch

ABSTRACT

This work details the design, assembly, and testing of a high temperature electron beam evaporator for equilibrated vapor phase evaporation of rock oxides for the purpose of astrophysical characterization of extrasolar planetary atmospheres. Infrared spectroscopy of high temperature SiO_2 atmosphere created through the electron beam evaporation technique and trapped by argon ice matrix isolation was performed to generate a reference spectrum against which absorption lines in stellar spectra taken during planetary transits can be compared. Studies demonstrate that water inclusions in milky quartz (SiO_2) can be used to create H_2O/SiO_2 equilibrated atmospheres within a Knudsen cell. Modeling of exoplanet spectra can be used to determine spectral photometry results as seen by astronomers for comparison with reference spectra collected.

KEYWORDS: exoplanet, hot super-earth, FTIR, electron beam evaporation, modeling

This abstract is approved as to form and content

_____

Dr. David Cornelison
Chairperson, Advisory Committee
Missouri State University

DESIGN OF HIGH TEMPERATURE EVAPORATOR FOR SPECTROSCOPIC STUDY OF EQUILIBRATED VAPOR PHASE MATERIALS

By

Yarden Bosch

A Masters Thesis
Submitted to the Graduate College
Of Missouri State University
In Partial Fulfillment of the Requirements
For the Degree of Master of Science, Materials Science

July 2015

Approved:

_____
David Cornelison

_____
Mike Reed

_____
Peter Plavchan

_____
Julie Masterson, PhD: Dean, Graduate College

TABLE OF CONTENTS

LIST OF TABLES

LIST OF FIGURES

INTRODUCTION

Extra-Solar Planets

Since the launch of the Kepler spacecraft in 2009 which revolutionized the field of extrasolar planetary research, more than 1000 confirmed extrasolar planets and 4000 more unconfirmed planet candidates have been discovered. Of these, 615 are rocky, Earth-like planets, 193 of which are 1000 K or hotter due to their close orbits (Figure 1).

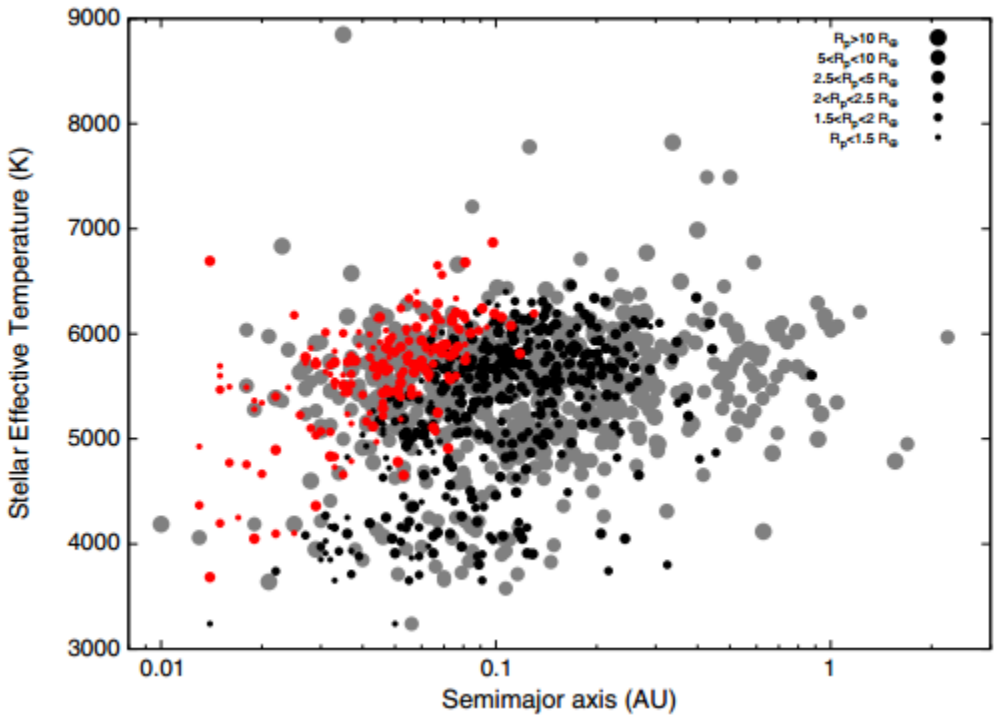

Figure 1. Hot super-Earths (red) relative to all Kepler planetary candidates (Miguel et al 2011). Size of dots indicates planetary radius.

Astronomers theorize that many of these planets have surface temperatures in excess of 2000 Kelvin due to their close orbits, giving them rock vapor atmospheres unlike anything found on Earth. One notable example is Kepler 10b, the first rocky

extrasolar planet to be discovered, shown in Figure 2. Kepler 10b's mass is 4.6 times that of Earth's and its radius is 1.5 times that of Earth's, but it orbits at only 1/60th of Earth's orbital distance, giving it a day temperature of 3316 K and a night temperature of 2600 K (Fogtmann-Schulz et al 2014). Rouan et al (2011) consider it to be a "Lava-ocean" planet, a category of exoplanets proposed by Léger et al (2011) which also contains CoRoT 7b, a widely studied rocky super-Earth with similar properties and an even more drastic temperature gradient between day and night. The extreme temperatures of the day side are thought to cause the melting of the rock surface and formation of a lava ocean, above which there might exist a thin atmosphere of rock vapors without clouds or volatile gases (Léger et al 2011). Other hot rocky super-Earth planets included in this classification are 55 Cancri e (Winn et al 2011) and Kepler 78b (Howard et al 2013). A listing of such planets can be found in Table 1.

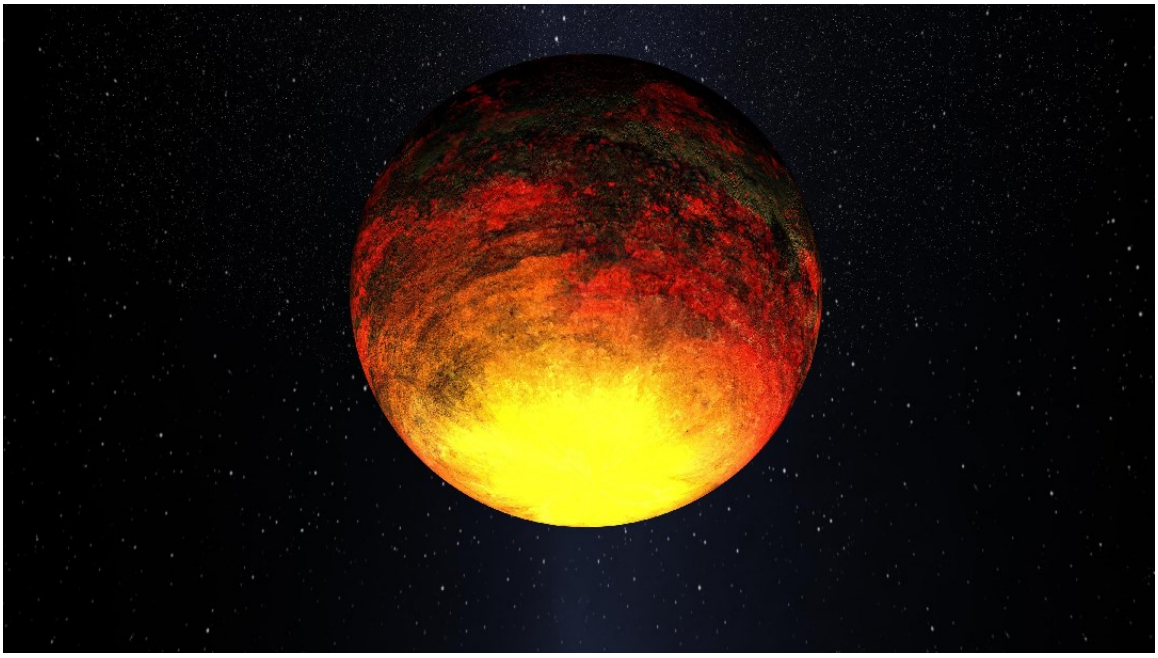

Figure 2. Artist's depiction of Kepler 10b (NASA/Kepler Mission 2011).

These extrasolar planets provide both a picture similar to the development of the early Earth and an entirely novel set of extreme conditions which are not very well understood. To get a better understanding on what takes place on such "hot Earths", it is necessary to determine their composition with a much greater degree of confidence than has previously taken place.

Table 1. Known super-Earth planets and their surface temperatures (Schaefer et al 2012).

	Orbital and Physical Properties of Known Transiting Low-mass Planets				
Planet	Mass (Earth masses)	Radius (Earth radii)	Density (g cm^{-3})	Orbital Radius (AU)	Surface Temperature (K)
Kepler-11 f	2.30	2.61	0.71	0.25	544
GJ 1214 b	6.55	2.68	1.88	0.014	555
HD 97658 b	6.40	2.93	1.40	0.0797	510-720
Kepler-11 e	8.40	4.52	0.5	0.194	617
Kepler-11 d	6.10	3.43	0.83	0.159	692
Kepler-11 b	4.30	1.97	3.10	0.091	900
Kepler-20 b	8.70	1.91	6.5	0.04537	1014
Kepler-18 b	6.90	2.00	4.9	0.0447	1179
CoRoT-7 b	7.42	1.58	10.4	0.0172	1810
Kepler-10 b	4.54	1.42	8.74	0.01684	1833
55 Cnc e	7.98	2.13	4.97	0.01564	1967

Atmospheres

With the large amount of new extrasolar planets being discovered, their composition has become a hot topic in astronomy. Studies have been done on numerous potential compositions for extrasolar planets using computer modeling and constrained

by known factors such as the density and temperature of the planet in question. A planet's bulk composition can be determined from its density, and its temperature can be approximated from its albedo and the distance to the star. Once these are known, the partial pressures of the planet's atmosphere can be modeled via the vapor pressures of the materials that compose its surface. Simulation of chemical interactions between those molecules at the ratios and temperatures specified determines the final composition. The MAGMA code, developed by Schaefer and Fegley, simulates the evolution of a planet's surface and atmospheric composition with time given a set of initial conditions and a temperature greater than 1000 K. A generalized plot of this data scaling with temperature can be seen in Figure 3. This code has been applied to a number of extrasolar planets discovered in the Kepler data.

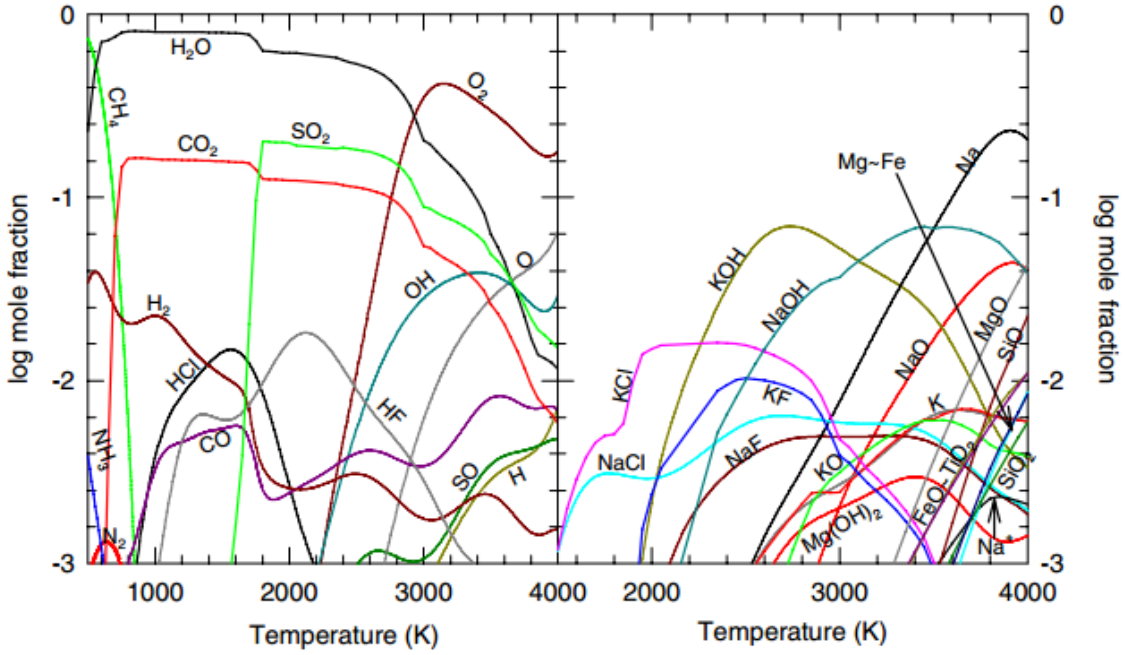

Figure 3. Atmospheric gas composition relative to surface temperature for a planet with Earth's composition, calculated using MAGMA (Schaefer et al 2012).

In the case of CoRoT-7b, whose day surface is thought to be a permanent lava ocean 45 km deep (Léger et al 2011) (see Figure 4), atmosphere is thought to be composed of surface rocks which are vaporized and sublimated. Assuming a specific komatiite mixture based on the metallicity of the parent star, Schaefer et al (2012) calculated the partial pressures of gases present in CoRoT-7b's atmosphere, the results of which are in Figure 5. Komatiite is an Earth magma which varies in composition; compositions commonly used in modeling can be seen in Table 2.

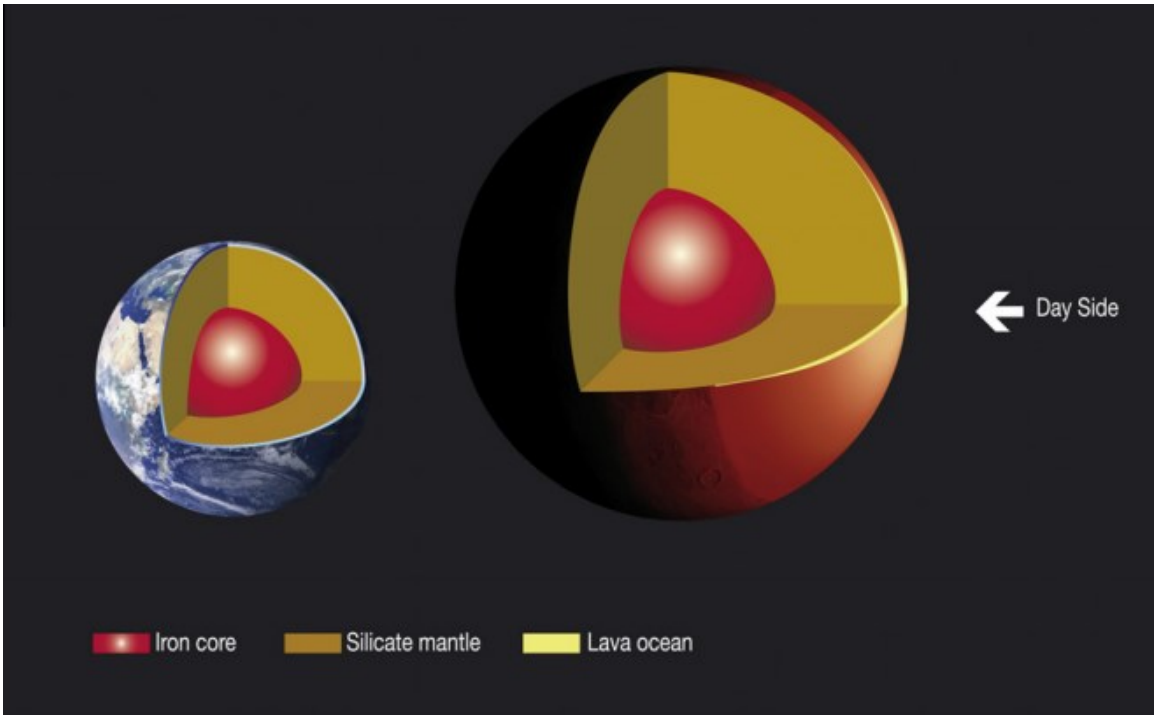

Figure 4. Model of CoRoT-7b's internal structure (Léger et al 2011).

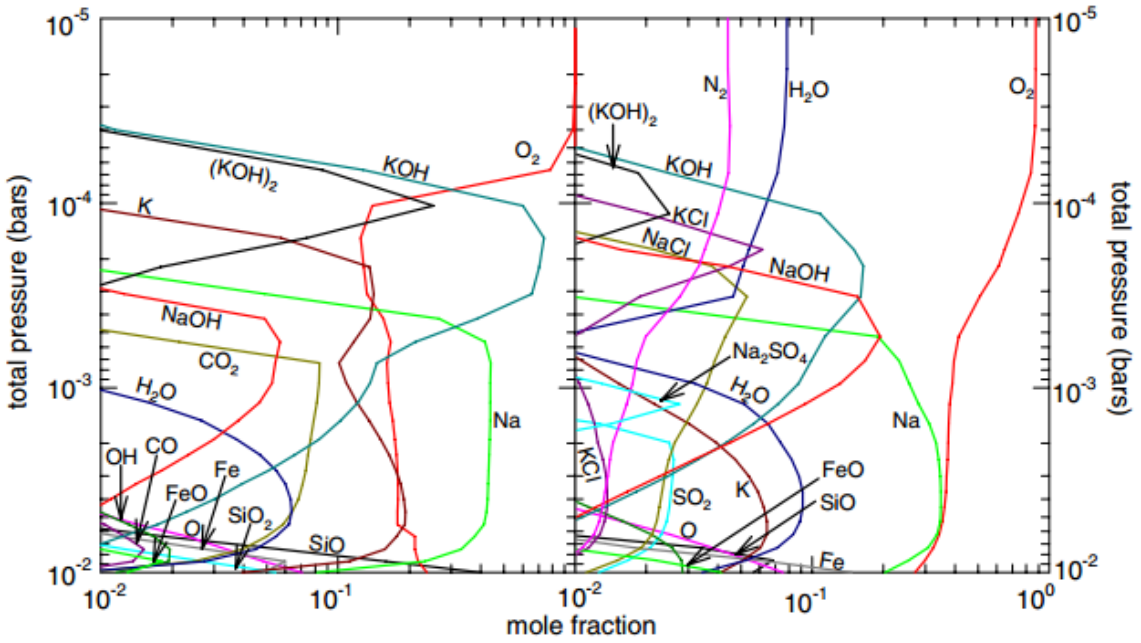

Figure 5. Atmospheric gas composition for CoRoT-7b assuming 2500 K temperature and 10^{-2} bar pressure for two alternate compositions, calculated using MAGMA (Schaefer et al 2012).

The same approach, taken for a number of other hot super-Earths, has interesting results: although a number of planets have atmospheres dominated by oxygen gas and monatomic constituents, four others are found with large quantities of silicate vapors in their atmosphere. Miguel et al (2011) studied the atmospheric composition of 193 hot super-Earths: rocky planets with masses below 10 times that of the Earth and radii below 2 times that of the Earth from the 2011 Kepler data set whose surface temperatures exceeded 1000 K. The physical parameters of these planets can be seen in Table 3.

Table 2. Elemental composition of komatiites used for kinetic chemistry simulations in codes such as MAGMA (Schaefer et al 2012).

Element	Bulk Compositions of Vaporizing Planets	
	Continental Crust (wt.%)	Bulk Silicate Earth (wt.%)
O	47.20	44.42
Si	28.80	21.61
Al	7.96	2.12
Fe	4.32	6.27
Ca	3.85	2.46
Na	2.36	0.29
Mg	2.20	22.01
K	2.14	0.02
Ti	0.401	0.12
P	0.076	0.008
Cr	0.013	0.29
Mn	0.072	0.11
H	0.045	0.006
C	0.199	0.006
N	0.006	0.88x10-4
S	0.070	0.027
F	0.053	0.002
Cl	0.047	0.004

Table 3. Hot super-Earth planetary candidates found by the Kepler mission (Miguel et al 2011).

Planet	Planetary and Stellar Parameters for *Kepler* Candidates with Radii Less than 2.5 Earth Radii and Temperatures Higher than 1000 K				
	Planet Radius (Earth radii)	Planet Temperature (K)	Orbital Radius (AU)	Star Radius (Solar radii)	Star Temperature (K)
KOI 69.01	1.6	1129	0.056	1.03	5480
KOI 70.02	1.6	1001	0.046	0.7	5342
KOI 72.01	1.3	1946	0.018	0.98	5491
KOI 85.02	1.7	1987	0.035	1.66	6006
KOI 85.03	2.0	1282	0.084	1.66	6006
KOI 107.01	2.1	1025	0.075	1.01	5816
KOI 112.02	1.7	1414	0.048	1.22	5839
KOI 115.02	2.2	1251	0.076	1.34	6202
KOI 117.02	1.3	1142	0.058	1	5725
KOI 117.03	1.3	1326	0.043	1	5725
KOI 123.01	2.3	1188	0.071	1.25	5897
KOI 124.01	2.3	1006	0.111	1.32	6076
KOI 137.03	2.3	1335	0.046	1.27	5289
KOI 139.02	1.2	1272	0.045	0.9	5921

To construct models, the planets were assumed to have a komatiite composition without volatile gases like hydrogen and nitrogen which are assumed to escape from the atmosphere at such high temperatures. Outgassing simulations for temperatures between 1000 and 3500 K result in a number of different atmospheric compositions (Figure 6). For surface temperatures below 2096 K, atmospheres are dominated by Na, O2, O, and Fe. Above 2096 K, SiO overtakes Fe; above 2460, SiO overtakes monoatomic oxygen; above 2735 K, SiO is more abundant than diatomic oxygen; and above 2974 SiO is the

most abundant atmospheric species. This is almost independent of planetary mass (given rocky planets). These simulation results can be reproduced in a laboratory setting for spectral analysis by heating the constituent parts in the proper percentages to the surface temperatures desired and maintaining equilibrium conditions.

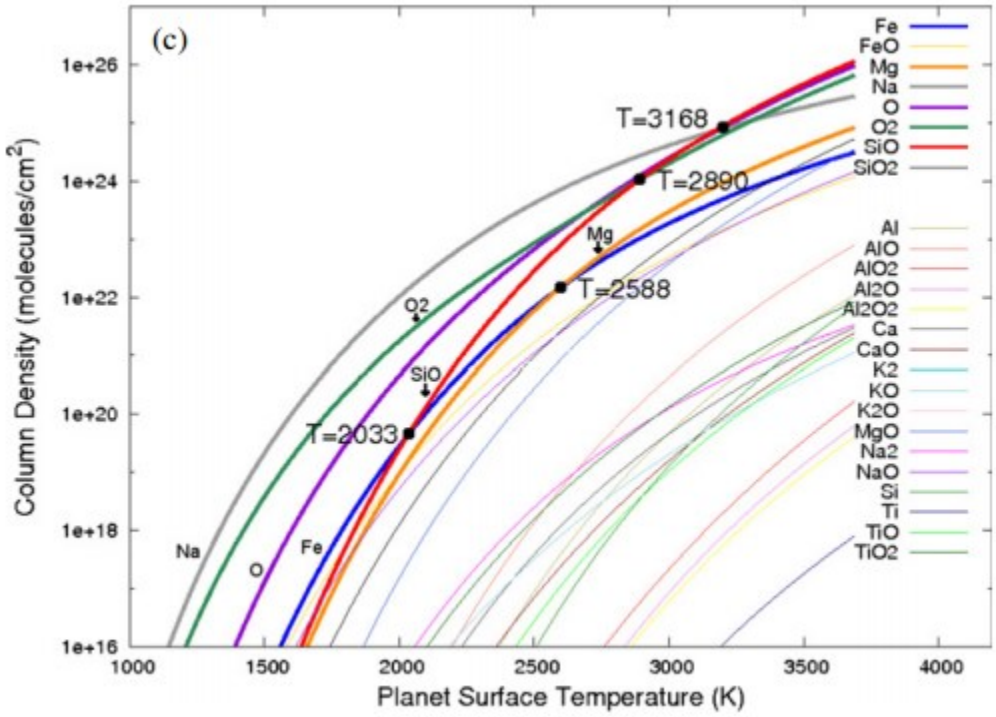

Figure 6. Partial pressures for atmospheric gases for a komatiite composition (Miguel et al 2011).

Knudsen Cell Theory

Knudsen cell effusion is a technique that allows for sampling of equilibrium vapor phases of materials necessary to mimic conditions on the planets, which are in a general state of equilibrium. A Knudsen cell consists of an isothermally heated evaporation crucible with a closed top and small orifice through which vapor can escape (Figure 7).

The size and shape of the orifice as related to the volume of the cell determine the closeness to an equilibrium state of the system (consisting of the crucible walls, the evaporant sample in the solid phase, and vapor) as well as the deposition profile.

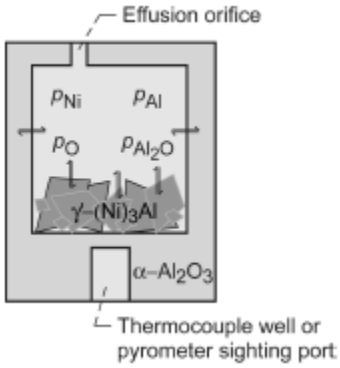

Figure 7. Simplified representation of a Knudsen cell (Copland and Jacobson 2010).

Evaporation flux from a free surface with an area A and temperature T is traditionally represented using the Hertz-Knudsen equation (Carlson 1967)

$$\frac{dN}{dt} = \alpha A(2\pi m k_B T)^{-1/2}(P^* - P) \quad (1)$$

Where P^* is the equilibrium vapor pressure of the evaporant, P is the ambient pressure working against evaporation, and the sticking coefficient α represents the fraction of evaporant molecules that do not return. In a Knudsen cell, the evaporant molecules will reflect off the entire surface area of the crucible except for the orifice, and evaporant molecules that pass through the orifice will never return. Thus, ideal Knudsen-cell flux is simply

$$\frac{dN}{dt} = A_o(2\pi m k_B T)^{-1/2}(P^* - P) \quad (2)$$

Where A_o is the cross sectional area of the orifice. With a real, finite length orifice, flux is multiplied by the Clausing factor W_C, which is the proportion of incident flux that

escapes due to the shape of the orifice. Molecules exit the orifice according to a cosine distribution dependent on the ratio of the length and radius of the orifice: as l/r increases, the Clausing factor decreases, such that an infinitesimal length yields a Clausing factor approaching 1. To produce this near-ideal effusion cell, a knife-edge orifice is used, providing a nearly uniform flux distribution. The disadvantage to this technique is that a larger proportion of evaporant flux to total evaporant material makes it more difficult to sample equilibrium conditions. To reduce the Clausing factor, a channel orifice (Fig. 8) can be used. This raises the probability that effusing molecules, particularly at high angles from the normal to the orifice, will have interacted with the orifice walls, so the molecular beam should not be sampled at high angles from the normal when using this method (Copland and Jacobson 2010). The resulting change in flux profile can be seen in Figure 9.

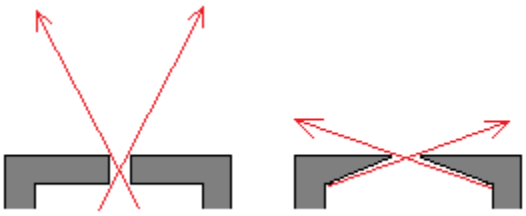

Figure 8. A channel orifice (left) allows fewer molecules to escape than a knife-edge orifice (right).

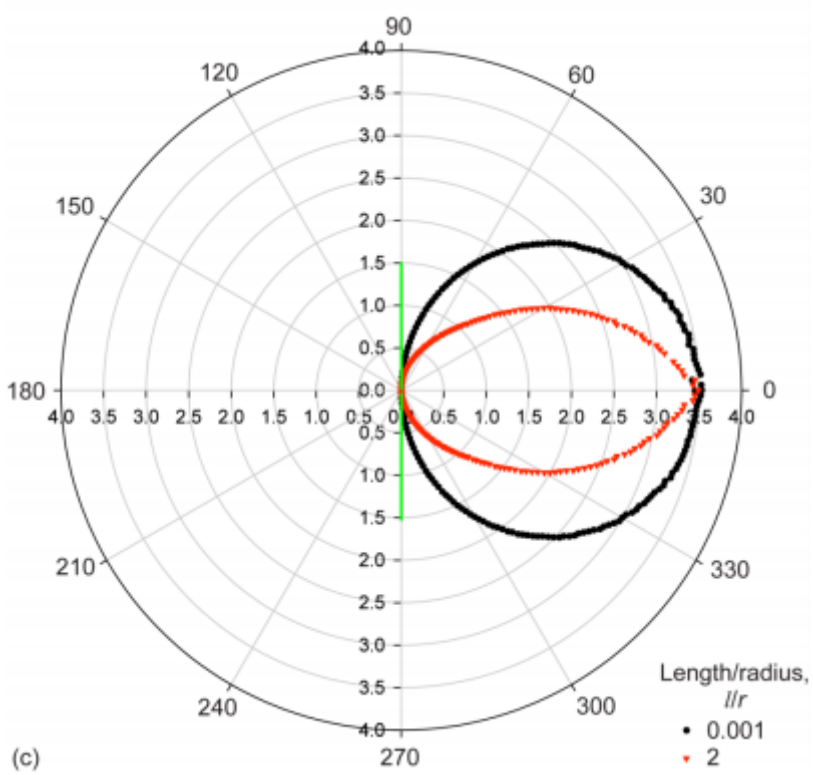

Figure 9. Distribution of molecules for a thin orifice (black) and a channel orifice (red), derived from Monte Carlo simulation (Copland and Jacobson 2010).

The factors which make a successful Knudsen cell design can be summarized through the Whitman-Motzfeldt equation (Hannay 2012):

$$\frac{P_e}{P_m} = 1 + \frac{W_C C}{D}\left(\frac{1}{\alpha} + \frac{1}{W_D} - 2\right) \tag{3}$$

Where P_e/P_m is the ratio of equilibrium to measured vapor pressure, C/D is the ratio of orifice surface area to the surface area of the cell side containing the orifice, and W_D is the Clausing factor for the vapor transport within the cell (non-unity in complex cells with inner and outer crucibles). In general, the method to obtain P_e/P_m near unity (in other words, an equilibrated system) is to reduce W_C by using a channel orifice and minimize C/D (less than 1/1000 is recommended). In addition, cell materials need to be

selected to avoid introducing impurities into the system. A typical material should be relatively inert, with a low vapor pressure at the temperatures used during effusion, so that minimal contamination occurs, such as Pt, Mo, W, Ir, Re (Miller and Armatys 2013). In designing our own system, we did not systematically alter C/D to find the ideal balance between flux and equilibrium, but used a fixed ratio. Varying C/D can be done easily by having crucible lids machined with different sized apertures, and is an area for future study.

Observational Work

The technique which will play the most significant role in future characterization of exoplanet atmospheres is spectroscopic or photometric measurement of the atmosphere. When a planet passes in front of its parent star, a small portion of the star is eclipsed by the planet, causing a dip in the intensity of the star called a transit. Similarly, when the planet passes behind the star (the secondary eclipse), light from the planet does not reach telescopes here on Earth. If the star is not variable, the star's intensity can be thought of as constant, while the planet's follows a sinusoidal pattern, with the largest portion of light reflected from the planet when it is almost directly behind the star and the least reflected when it is directly in front of the star (neglecting eclipses). The phases of an exoplanet are shown in Figure 10. In addition, all planets generate a quantity of their own light through blackbody emission. Adding each contribution to these creates the full light curve which is can be measured over time with a telescope (Fig. 11). A star has a spectrum similar to a black body, with dips corresponding to the available electronic transitions within the atoms. When that starlight passes through a planet's atmosphere,

absorption lines corresponding to the planet's atmospheric composition are added to the spectrum. An example of this effect as seen through Earth's atmosphere, which contains the infrared active molecules carbon dioxide and water (Figure 12).

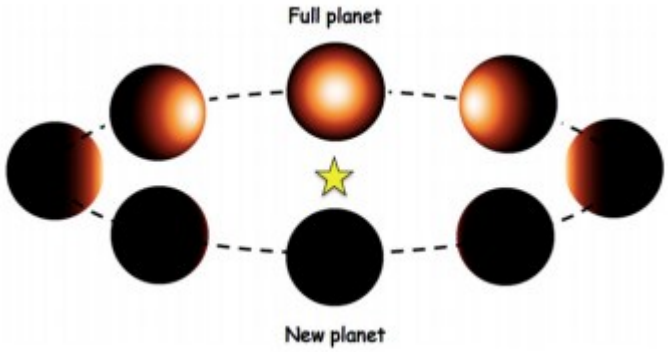

Figure 10. Planetary phases indicating detectable reflected light (Rouan et al 2011).

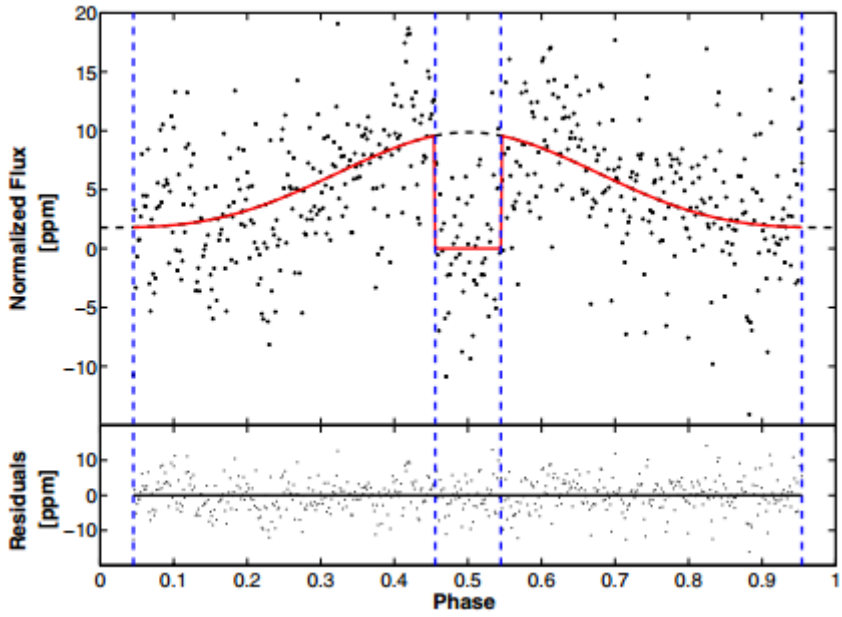

Figure 11. Planetary transit of Kepler 10b (Fogtmann-Schulz et al 2014).

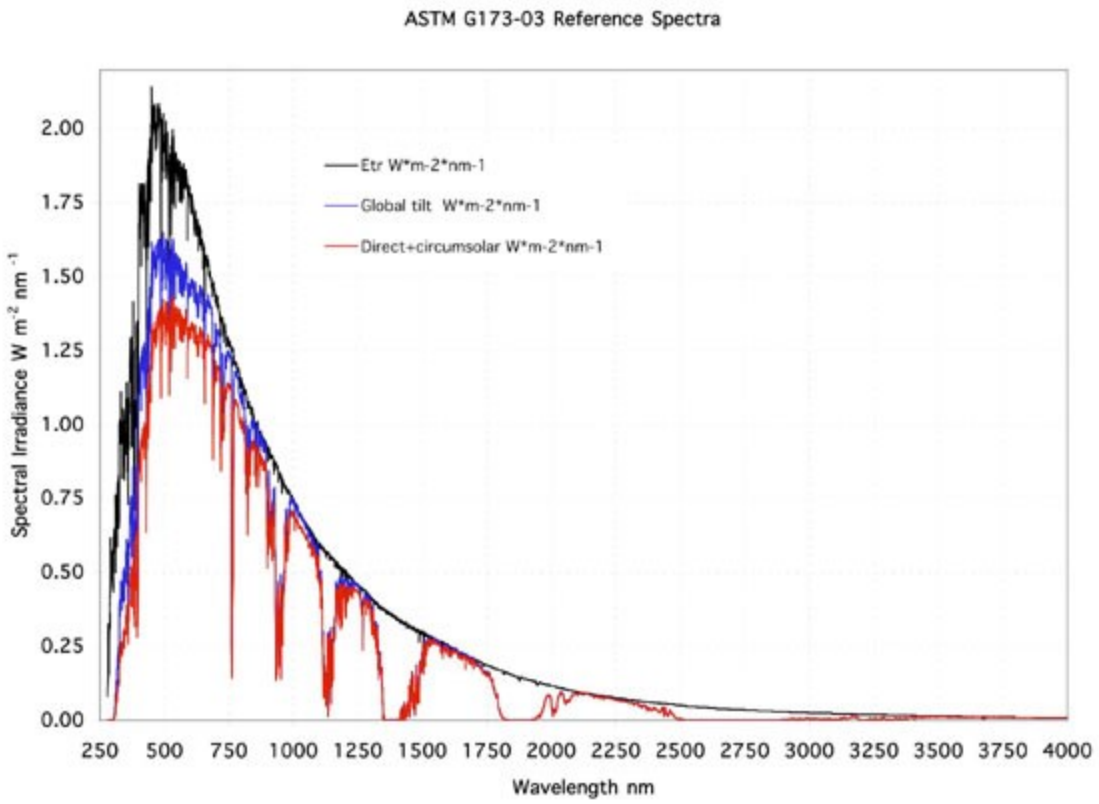

Figure 12. Spectrum of sunlight (black) and sunlight that has passed through Earth's atmosphere (red) (ASTM 2012).

In other words, the spectrum recorded during a transit is the spectrum of the star and the star alone, while spectra recorded when the planet is not in front of or behind the star contain information from the planet. If the secondary eclipse can be resolved, it contains the pure star spectrum with no added light from the planet or subtracted light from the eclipse. By comparing these spectra, an atmospheric spectrum for the planet might be obtained. Limitations to this technique are numerous, however. Because stars are many orders of magnitude brighter than planets, resolving the planet's spectrum is difficult and requires a great deal of noise reduction. Typically this involves binning or collecting a smaller number of observations using various filters and approximating the

spectrum in this manner (photometry). An example of the photometric technique is shown in Figure 13.

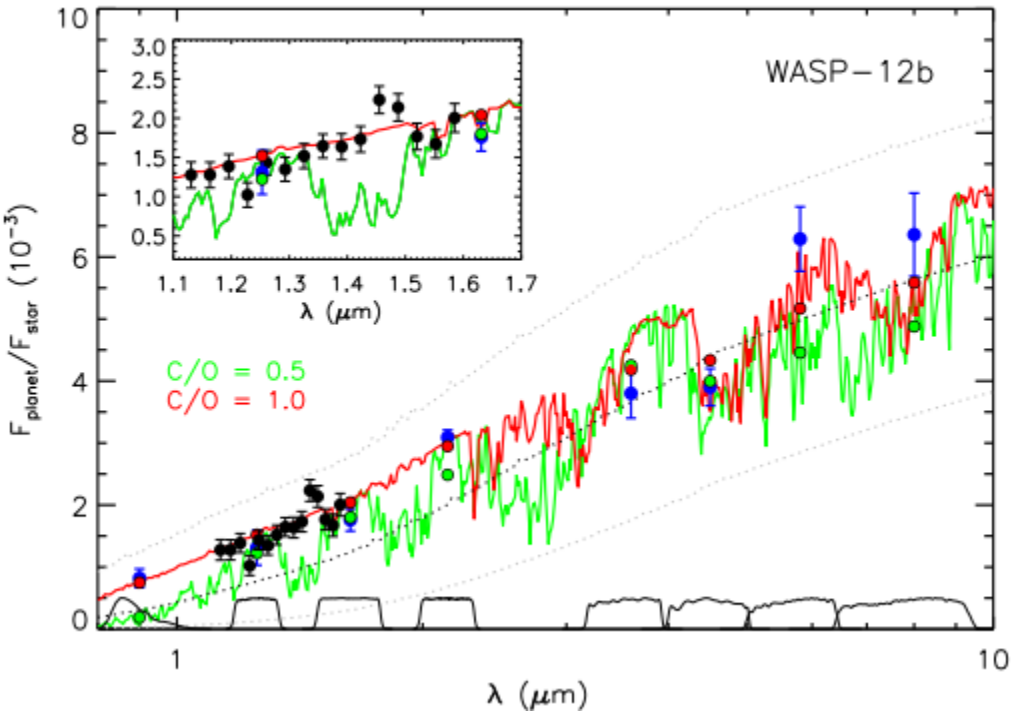

Figure 13. Example of the use of photometry (blue points) to attempt to fit to model compositions (green and red lines) for the hot Jupiter type exoplanet WASP 12b (Madhusudhan 2012). Filter bands used to collect the blue data points can be seen at the bottom of the figure in black.

Essentially, photometry is the collection of light through various filters, each with a limited band of transparency. Each of the points in Figure 13 corresponds to the intensity of light collected through the filter whose transmittance is pictured at the bottom of the figure. Photometry has a much lower spectral resolution than a conventional spectrometer as light of all of the wavelengths in each filter band are sampled together; however, this also means greatly improved signal, which is a necessity when measuring small, distant light sources.

Many of these hot super-Earths have atmospheric conditions that have never been studied here on Earth, and have only theoretical reference spectra, so there is a need for lab reference data to compare such observations with in order to verify models. In the lab, similar spectra could be collected by passing a beam of light through a gas and into a spectrometer, imitating the path of the star's light through the planet's atmosphere (Fig. 14).

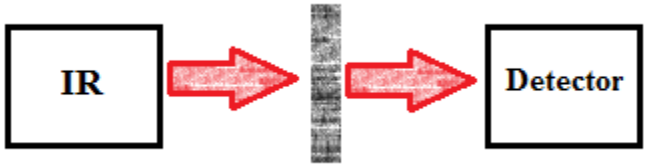

Figure 14. Path of spectrometer beam.

As light passes through the gas, photons with a wavelength λ corresponding to a molecular vibration with an energy hc/λ present are absorbed by the gas and not picked up by the detector. The diminished intensity in the transmission spectrum forms a series of signature peaks known as absorption lines. Absorption follows the general form:

$$I(\lambda) = I_0(\lambda)e^{-\alpha(\lambda)t} \quad (4)$$

Where t represents the thickness or density of the gas being studied.

The specific technique we use in the lab is Fourier transform infrared spectroscopy (FTIR). The difference between FTIR and other spectroscopic techniques is that FTIR measures all wavelengths of light at once, taking advantage of the Fourier transform, yielding great advantages in resolution, scan speed, and signal-to-noise ratio. An optical beam passes through a beam splitter and becomes two beams, one with a fixed path and one reflected off a movable mirror (Fig. 15). The beams are brought back

together and sent towards the sample with some phase difference determined by the movable mirror's position, reflecting off it or passing through it depending on the instrument and type of scan, and finally sent to a detector. The mirror moves back and forth, and the intensity of the signal received by the detector goes up and down accordingly as the beams interfere constructively or destructively (Smith 2011).

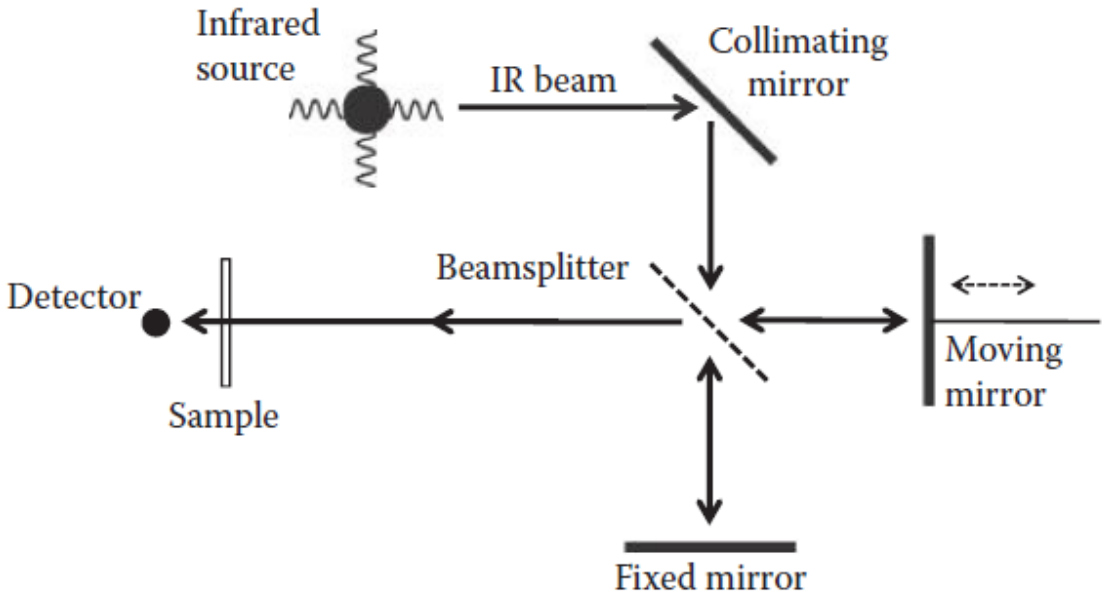

Figure 15. Diagram of an interferometer used for FTIR spectroscopy (Smith, 2011).

This signal, measured as a function of phase difference, is called an interferogram. By performing a Fourier transform, a mathematical technique which converts information from time space to frequency space, on the interferogram, we obtain intensity as a function of inverse distance (spatial frequency, commonly called wavenumber k and measured in inverse centimeters):

$$I(t) = \frac{1}{\sqrt{2\pi}} \int_{-\infty}^{\infty} G(k) e^{ikt} dk; \;\; G(k) = \frac{1}{\sqrt{2\pi}} \int_{-\infty}^{\infty} I(t) e^{-ikt} dt \tag{5}$$

Here $G(k)$ contains the information in frequency space. Wavenumbers correspond to the wavelength of the light that reaches the detector, so by recording the intensity of a single oscillation of the mirror, we can obtain a complete spectrum of absorbed or transmitted light, as limited by the source, the detector, the beam splitter, the medium the beams travel through, etc., as shown in Figure 16.

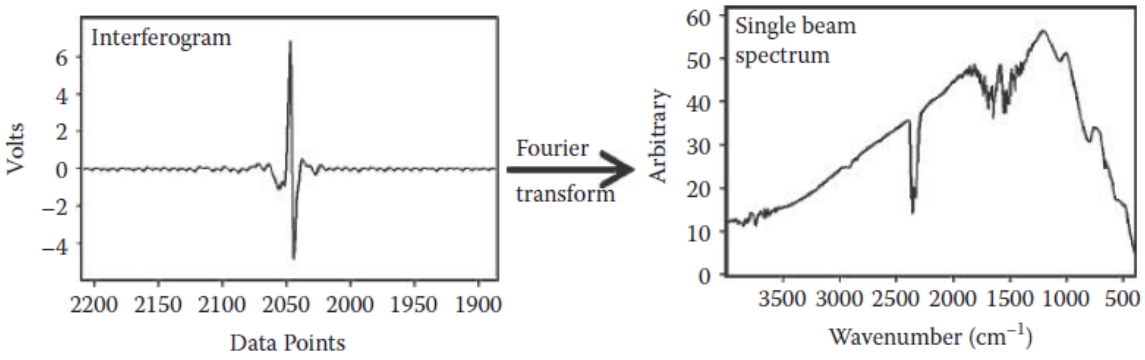

Figure 16. Example interferogram and Fourier transform spectrum (Smith, 2011).

Although measuring the spectra of the molecules in the gas-phase would be ideal, in practice it becomes a difficult task when the density of the gas is low: recall that line depth is a function of the number of molecules intersected by the beam (Equation 4 above). Matrix isolation is a spectroscopic technique used to isolate a greater quantity of sample molecules for convenience of analysis. In general, matrix isolation refers to the mixing or co-deposition of sample molecules with an inert or unreactive gas onto a sufficiently cold surface that the unreactive gas traps individual sample molecules within an ice "matrix", separated from one another by inert materials so that they cannot interact. This has the effect of freezing the sample in time: it cannot continue to react, but remains in whatever state it was when it entered the ice, allowing gases that would

ordinarily be quite difficult to study, such as an equilibrium vapor, which rapidly ceases to be equilibrated once it interacts with anything else, or intermediate compounds in reactions with very short lifetimes, neither of which could be analyzed at a very high resolution or accuracy with even a top-of-the-line modern spectrometer. The other main advantage to matrix isolation is that a low density gas sample, which might be impossible to resolve with a spectrometer, can be grown onto a substrate to improve signal without leaving the gas phase.

When performing matrix isolation, choice of matrix gas becomes very important. Minimizing interactions between sample and matrix gases is key because any interactions mean the data recorded will no longer be an accurate representation of the original gas phase prior to isolation. A gas must be chosen which is stable, frozen, and inert at the substrate temperature used. The most commonly used gases are lighter noble gases and nitrogen, although heavier, higher boiling point noble gases like krypton and xenon can be used where substrate temperatures are limited. In some cases, matrix gases are chosen that will react with only specific molecules. In all cases, however, optical transparency must be considered. Many frozen solvents are opaque in the infrared, blocking out part or all of the desired spectrum. This makes monoatomic and elemental diatomic gases, which are transparent to IR, ideal. It must be noted that some gases which are transparent at room temperature have an infrared signature in a low temperature solid phase, such as nitrogen.

Similarly, preventing diffusion through the matrix is crucial. This in turn means that substrate temperature is a parameter that must be carefully controlled. The desired temperature depends on the matrix gas used: for neon or hydrogen gas, a temperature of 4

K or less is necessary. This requires a special cryostat known as a flow cryostat, which cycles expensive and difficult to handle liquid helium through the cold head itself. Other gases will freeze out at higher temperatures so a closed cycle cryostat, which uses helium gas and a compressor to reduce the temperature of the cold head to 6 K or less (depending on the mass of the cold head), using the Gifford-McMahon cycle.

Although isolating sample molecules within a matrix gas is very advantageous for performing spectroscopy, the technique brings with it a number of disadvantages. The first is that the molecular species to be analyzed must be reduced by several orders of magnitude in quantity as compared to the co-deposited matrix gas. A ratio of 1,000 argon atoms to 1 sample molecule is recommended. This generally means restrictions on the evaporation rate of the sample. Another factor that must be taken into consideration is that ice matrices, particularly those composed of noble gases, are poor heat sinks, meaning the effective isolation of the sample will decrease with the thickness of the ice. In addition, energetic molecules might undergo decomposition if not immediately frozen out. Another problem with matrix isolation is its tendency to detect disproportionate amounts of dimers and higher order coordinated molecules, particularly with molecules that are extremely polar. This can be alleviated somewhat by further increasing the ratio of host gas to sample gas but this brings with it still more reduction in signal. Decreasing substrate temperatures may also be of limited use. One trick, which may not be feasible in many cases, is to impart additional energy upon the sample gas molecules prior to their entering the matrix to break up any aggregates. However, this violates the equilibrium conditions that were desired (Bally 2004). If this effect does take place, correcting it will be a part of future work.

Another issue with matrix isolation, is the tendency for some molecules to be affected by the matrix gas in ways that are visible in the spectra. Some samples will form strong chemical complexes with noble gas atoms, sometimes with such strength that the molecule and the matrix gas atom have effectively formed a chemical compound. As infrared spectroscopy studies the vibrational modes of the bonds between the atoms in the molecule, an infrared spectrum of such a complex will be different from that of a truly pure equilibrated sample with no matrix gas atoms present. For example, the presence of a xenon matrix gas induces a 78 cm^{-1} blueshift in BeO when XeBeO complexes form (Nakayama 2012). It is still possible to determine the abundances of species present from the spectra, however, as no new spectral lines are formed, only some shifting of the original lines takes place.

ENGINEERING

High Temperature Evaporation Overview

The bulk of the work done for this study consists of the design, construction, and characterization of a high temperature evaporator using Knudsen cell effusion to obtain the desired equilibrium conditions of astrophysical interest. Considerable effort went into the design and construction of our system, not all of which was successful; the final implementation will be detailed below. Knudsen cells are typically heated either with a resistive heating element or with an electron beam. Resistive heating is the simplest of all vapor sources. A basic resistive heater consists of a support material which contains the sample material to be heated. Large electrical current flows through the support, increasing the temperature until the point at which the sample material vaporizes. A more complex resistive heater might use a wire filament wound around a crucible containing the sample to be evaporated (instead of passing current through the crucible itself) and any number of heat shields and shutters for temperature and deposition rate control. Resistive heaters generally do not provide uniform deposition, but this can be counteracted by using a Knudsen cell or by placing the substrate on a rotatable flange driven by a motor. Materials used in the construction of resistive heaters are generally high melting point, low vapor pressure materials that are not expected to react with the sample, e.g. tungsten, tantalum, molybdenum, graphite. The use of inner crucibles or a surrounding heater wire can offset undesirable electrical properties of a nonreactive material used to hold the evaporant sample (typically a ceramic such as alumina, zirconia, etc).

The heating power of a resistive heater can be described simply by the relation $P = I^2R$, where I is the current passing through the heating element and R is its resistance. Limitations to the resistive heating technique are derived from this relation: a high heating power requires truly large amounts of current. If, for example, the heating element has a 0.1 ohm resistance and 250 watts of heating power is desired, 50 amps of power must be supplied continuously to the heater. Not only do high currents require expensive power supplies and safety precautions during operation, special wires and feedthroughs that can withstand the current must be used for every connection, and the heating elements themselves can become massive. This means that a very large amount of heat is dumped into the system at every step of the way, and care must be taken to ensure the cooling of feedthroughs and anything else that might be heated by accident, as heating power is lost in all directions when filaments radiate instead of directly contact the sample (necessary for isothermal heating). Common solutions are to surround the heating elements by heat shields or a water cooling jacket. Another thing that must be kept in mind when operating a resistive heater is the temperature change in resistivity of the heating element material. As the temperature of the heating element changes, its resistivity can change, effectively changing the target temperature. This could cause a temperature target not to be met or a runaway heating effect, so resistive heaters must be ramped gradually to take into account temperature changes.

Resistive heating is typically used at lower temperatures, as heating power scales with current squared requiring massive, water-cooled feedthroughs for higher temperature applications. It is also much less efficient than e-beam heating because the radiative heat cannot be focused on the Knudsen cell: much of the power radiates

outwards, requiring heavy heat shielding. However, resistive heating has the advantage of avoiding electrical arcing or ionization within the chamber and the general dangers of the high voltages required for e-beam heating. The heating source for a Knudsen cell must provide isothermal heating around the cell. A common technique is to place the Knudsen cell within a long tube furnace, but this has the disadvantage of a very long working distance for the molecular beam, challenging for our applications. Another method is arrange multiple heat shields around the cell, which might ensure uniform heating (Sree Harsha 2005). Materials such as Ta and W are commonly used for heat shielding due to their low emissivity (Shukla et al 2004). This has the disadvantage of effectively creating a second Knudsen cell surrounding the first, where the shielding elements interact with any vapor which exits the orifice at a high angle to the normal, constituting a secondary contaminant flux (Jacobson et al 2002). This design is shown in Figure 17.

A more efficient heating technique is electron beam evaporation. An electron beam evaporation source consists of an electron source (cathode) and the evaporation material (anode). The electron source is generally a “hot cathode” thermionic emission source, although any stable electron source can be used. Electric and magnetic fields are used to direct emitted electrons to the anode, which is heated by electron bombardment. When an electron strikes the surface of the anode, its kinetic energy is converted into heat. This direct heating, as opposed to the indirect heating of a resistive wire element, is far more efficient and so greater temperatures can be obtained with minimal contamination and heating issues. For this reason, electron beam evaporation

sources are preferred over resistive heating sources at high temperatures. Electron beam evaporators have been verified to produce heating of up to 2500 ºC (Akishin 1967).

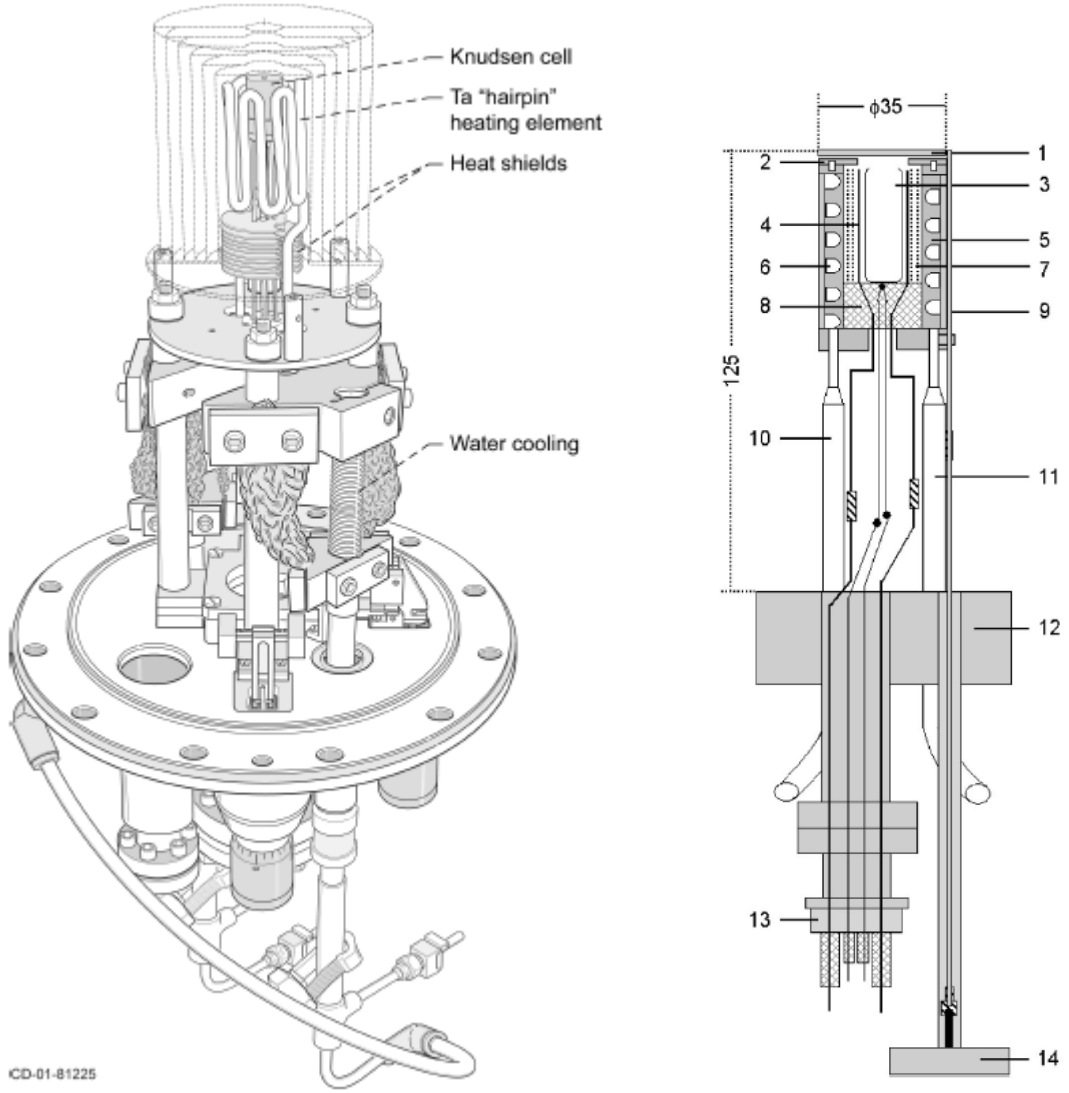

Figure 17. Resistively heated Knudsen cell designs incorporating Ta heating elements, heat shields, and water cooling. Left: (Copland and Jacobson, 2010); right: (Shukla et al, 2004).

The heating power of a simple electron beam evaporator is given by $P = V_A I_E$, where is the bias voltage of the anode and is the electron emission current (not to be confused with the current passing through the cathode, which is also an important

parameter). Unlike a resistive heater, therefore, an electron beam evaporator can reach a desired heating power by either varying the emission current or by varying the bias voltage (or both). This allows for a great deal in flexibility in the selection of power supplies and eliminates the need for heavy duty water cooled high current feedthroughs. Assuming that a suitably high voltage power supply is obtained, the limiting factor then becomes the emission current that the evaporator can provide. To follow up on the previous example of 250 watt heating power desired, a bias voltage of 1 kV will require 250 mA of emission current; but this power can also be achieved with a bias voltage of 5 kV and 50 mA of emission current, or 500 V and 500 mA of emission current, depending on the power supplies and emission sources available. In general, a high bias voltage is preferred over a high current because high currents generate excessive heat where heat is not desired, possibly leading to contamination issues or even melting of the instrument, and decrease the lifetime of emission sources.

Suitability of an electron source is determined by its stability, its durability under various conditions, and the current required to produce the desired emission current. In general, “hot cathode” electron sources consist of a fine metal wire. Passing moderate amounts of current through the wire heats it up, and this gives electrons sufficient energy to overcome the work function of the wire and exit the cathode, at which point they are attracted to the anode by the electric field, a process known as thermionic emission. Materials with a lower work function require a lower temperature to begin emitting electrons, making them more desirable. In addition to having a low work function, an ideal filament material should have a high melting temperature and low vapor pressure. This makes refractory metals such as tungsten, molybdenum, etc

desirable as filament materials. An emission surface's work function can be further lowered by coating with a thin rare earth or alkaline earth metal oxide layer or by adding a small quantity of thorium, lanthanum, yttrium, cerium, etc throughout the filament. The most commonly used filament material in electron sources is thoriated tungsten, which has a work function of only 2.6 eV (Berman, 2014). The shape of the material also plays a role: a single crystal which ends at a point has much greater emission than a loop of wire, but a loop of wire surrounding the anode will provide a more uniform distribution of electrons than a tip facing the anode. A final factor is the reactivity of the cathode. Thoriated tungsten, for example, is very susceptible to oxidation at pressures of 10^{-5} torr or above and cannot be operated at all at pressures greater than 10^{-3} torr. Filaments can be shielded from the higher pressures of the evaporation crucible by placing them a distance apart, but greater distance means the electric field will need to be stronger (higher anode voltage).

Similarly to the cathode, the anode needs to have certain properties if the evaporation is to be successful. First, the material used must be highly electrically conductive, as it must supply a bias voltage of 1 kV and channel the electron emission current to ground. Second, if the evaporation crucible is not directly water-cooled, the anode material must be durable under high temperature conditions: low vapor pressure, high melting point refractory metals are ideal. If the evaporation crucible is water-cooled, the material needs only to be unreactive with the material held within. The decision whether or not to attach a cooling block to the anode is dependent upon the maximum temperature desired; high temperature evaporators use only a cooling jacket surrounding the unit, with no contact to the anode, whereas low temperature evaporators

can afford to cool the entire instrument. Third, the anode's connection is the primary cause of heat loss from the crucible, so an effort should be made to minimize heat loss for high temperature applications. Using narrow connections or materials which poorly conduct heat for contact points can help in this case. Lastly, the evaporation crucible itself must also have these properties. Crucible materials are chosen based on the material to be evaporated and the temperature they must withstand, but in an electron beam evaporator there is the additional constraint of needing to be electrically conductive.

Temperature measurement of a Knudsen cell is challenging for several reasons. First, a thermocouple in contact with the crucible will act as a heat sink. The greater the ratio of thermocouple mass to crucible mass, the greater the problem. Second, the hot junction can act as a source of contamination in both directions. Pt/Pt-Rh thermocouples, commonly used for high temperature studies, will readily interact with metal vapors, introducing contaminants to the chamber while simultaneously altering the thermocouple and requiring frequent recalibration. An alternative is to use pyrometry, which has no thermal or chemical interaction with the Knudsen cell. This requires a direct line of sight and, depending on the temperature range, carefully selected window materials. Windows used for pyrometry need to be cleaned regularly as any line of sight to a hot crucible means molecular flux is bound to reach the window. Temperature measurements can be checked for accuracy by observing the melting of a well-known sample such as gold or copper (Copland and Jacobson, 2012).

High Temperature Evaporator Design

Electron beam evaporation was chosen due to its advantages in high temperature heating, and an evaporator was designed, assembled, and tested in-house. Initial plans called for the use of commercially available e-beam units, but after extensive work it was determined that these were insufficient: typical commercial units were unable to provide the desired temperatures and lacked the open geometry necessary to make adjustments to the design. The decision was made to construct a custom e-beam heater capable of achieving the desired high temperatures. An 8" steel flange was used for the base, with the anode rod mounted on an SHV mini feedthrough in the center. A 2-pin mini feedthrough for the cathode entered the flange to one side of the center, and a glass window on the opposite mini port for sighting an optical pyrometer. The entire base flange was inserted into an 8" to 10" flange on which a water cooling jacket was attached. Around the anode, molybdenum rods were used to construct a scaffold, with molybdenum discs with the centers cut out used to add stability. At the top of the scaffold, a 0.015" tantalum sheet was used to hold the posts to hold the cathode. Molybdenum and tantalum were chosen for use as a scaffold material because of their low vapor pressure and high melting point; a material such as stainless steel might outgas when exposed to the high temperatures within the evaporator and contaminate the sample. The posts used were alumina/molybdenum single pin feedthroughs from MDC Vacuum Products LLC, which electrically isolated the posts from the scaffolding (Fig. 18). The small diameter and short length of these posts is critical to the design: early designs using rods the length of the evaporator experienced considerable heat loss in the filament electron source and barely generated sufficient electron flux for heating.

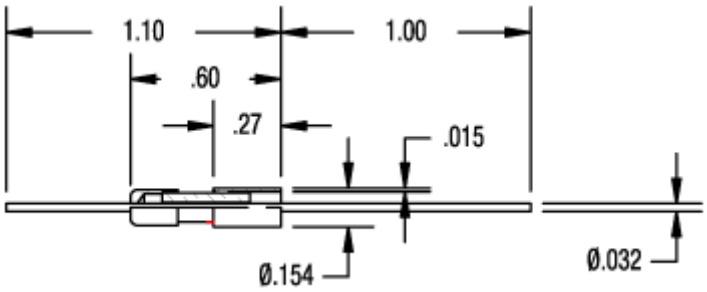

Figure 18. Feedthrough pins used to isolate cathode from scaffolding. The inner conductive material is molybdenum. Alumina is used to isolate the post from the adapter set into the top plate.

Fused to the posts was an iridium ring filament provided by the Fredericks Company. The ring filament is 2 cm in diameter. The diameter of the filament affects the strength of emission current provided because the closer the cathode and the anode are, the stronger the electric field applied to the cathode. The 2 cm size was chosen to avoid contact with the 8 mm outer diameter crucible, which suffered from considerable lateral oscillation in early stages of the design. A coating of thoria (ThO_2) was applied to the filament to lower its work function from 5.27 eV to 2.7-2.96 eV (Berman, 2014). This makes the thermionic emission rates of the iridium filament comparable to those of a thoriated tungsten filament (2.6 eV). Welding tabs were attached to either side of the loop to make resistance welding to the posts easier. The design is shown in Figure 19. The cathode pins were connected to the cathode feedthrough in the base flange by two 0.25 mm tungsten wires from each pin, using alumina fish spine beads to electrically isolate the wires from the scaffolding. During early testing, thoriated tungsten wire loops were used in place of thoria-coated iridium due to the cheapness and availability of thoriated tungsten; however, contamination issues that resulted from the use of thoriated tungsten necessitated the use of the iridium ring filament for the cathode.

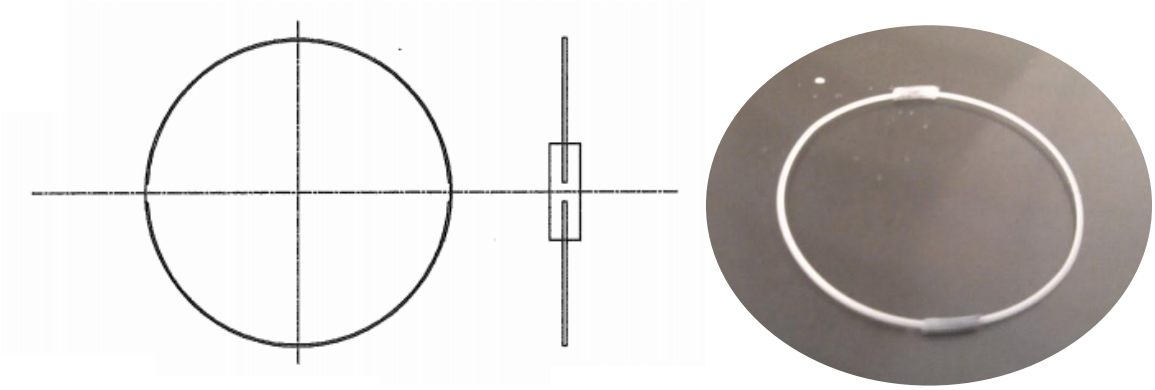

Figure 19. Top and side views of hot cathode filament design (left) and completed filament (right).

The anode consisted of a series of tantalum rods held together by barrel connectors to provide an adjustable height. At the base, the anode rod was connected to an SHV (safe high voltage) feedthrough by another barrel connector. Tantalum was used for its high electrical conductivity coupled with relatively slow heat transfer and high melting temperature. At the height of the top plate of the scaffolding, a feedthrough adapter was attached. This adapter was pressed in the center hole on the plate to dampen oscillations in the center rod. At the top of the center rod, with the middle aligned with the cathode filament, a crucible was attached through a press-fit.

Crucibles were machined from refractory metals by Missouri State University's in-house machinist (Figure 20). Tantalum and molybdenum crucibles were manufactured due to their high melting point and low vapor pressure. However, it was discovered that those materials (particularly molybdenum) are prone to oxidation, and the high oxygen environment of the evaporator caused a contamination signal produced in part by the crucible. This is a problem to be solved in future designs.

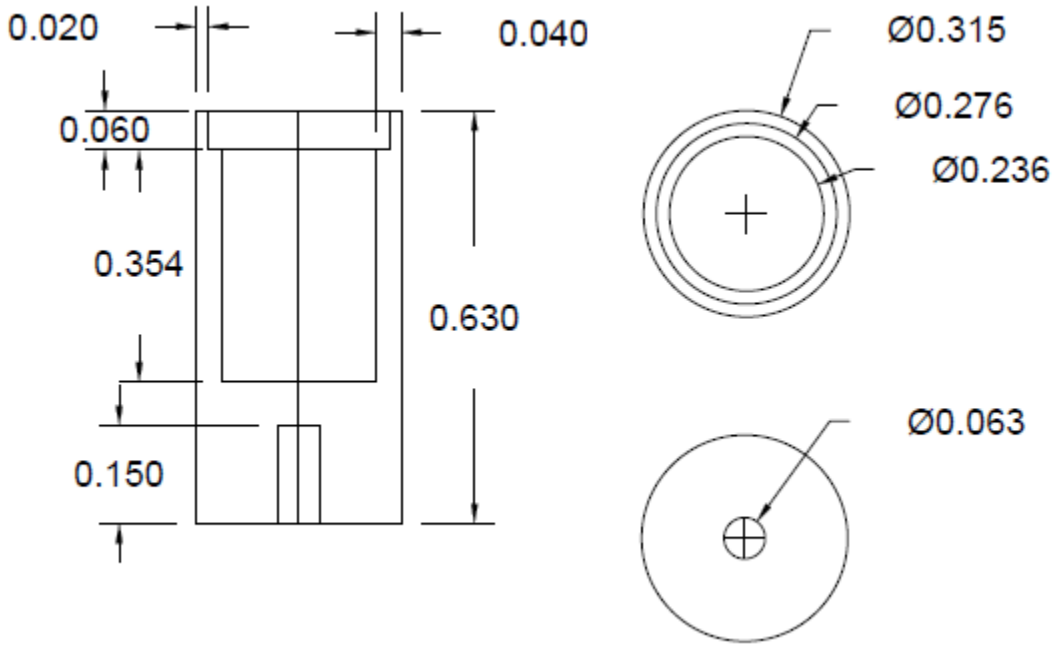

Figure 20. Side, top, and bottom views of evaporation crucible.

The crucible's mass needed to remain as small as possible in order to reach the highest possible temperature. A crucible mass of 6.5 g was used. After addition of the lid, this mass increased to 7.1 g, and heating performance decreased as a result. The addition of the lid also caused a drastic decrease in the amount of evaporant flux. However, the lid was vital to achieving proper Knudsen cell performance, as an open crucible is far removed from an equilibrium environment. A 1 mm orifice was drilled into the lid. The underside of the orifice was widened into the profile shown in Figure 21. The crucible and rod, being mounted on a mini (1.33") port in the base flange, could be lowered out separately, allowing for the crucible material to be changed without pulling out the entire evaporator. As high temperature evaporation causes a melting of the materials inside the crucible, crucibles were not truly reusable. Even after drilling out

the material remaining and using ultrasonic cleaning or an acid etch bath, some small mass of sample would remain in the crucible walls. For this reason it is necessary to manufacture a fresh crucible for each material sampled, or to use crucibles that can be fully cleaned.

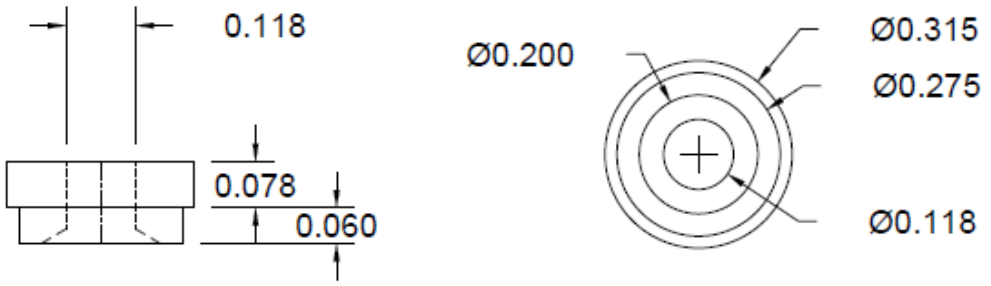

Figure 21. Side and top views of evaporation crucible lid.

After extensive testing, a 1.5 kV, 300 mA constant voltage power supply (Glassman Series EJ) was selected to drive the anode, and a 32 V, 72 A switching power supply (GW Instek PSW 32-72) for the cathode. The cathode supply can be operated in either constant voltage or constant current mode, but at high emission currents a positive feedback loop can develop in constant current mode where the high anode temperature radiatively heats the filament, lowering its resistance. The constant current provided which, with no radiative transfer, would reach the set temperature, instead has an additional effect of raising the temperature of the filament, leading to increased electron emission. This further increases the temperature of the crucible in turn and causes the process to continue. This runaway heating can be avoided by operating in constant voltage mode where the two causes of filament temperature act in opposition.

Care was taken to electrically isolate both the cathode and the anode from the scaffolding (grounded to the chassis) and from one another, using feedthroughs with alumina insulation material and alumina fish-spine beads. Once outside the vacuum chamber, however, the negative terminal of the anode supply was connected to the same ground as the supplies and the chamber, completing the circuit and preventing any charging from taking place. The circuit is shown in Figure 22.

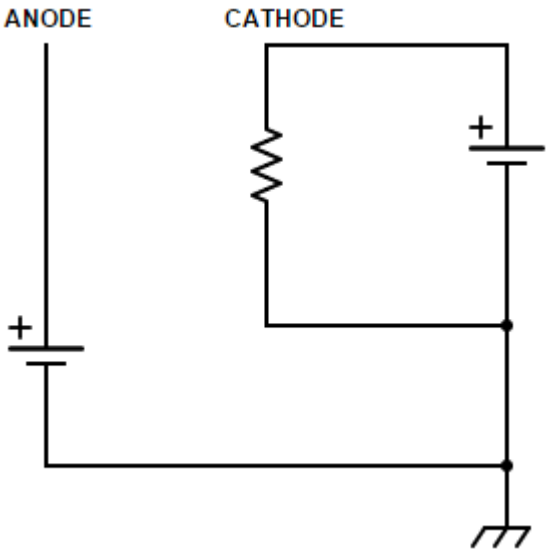

Figure 22. Circuit diagram of electron beam evaporator.

Testing of High Temperature Evaporator

A test chamber (Figure 23) was assembled for preliminary operation of the high temperature evaporator. This chamber was capable of reaching 10^{-10} torr when fully evacuated and with the cryostat cooled. It contained ports for the cryostat, residual gas analyzer, gas manifold, evaporator, ion gauge, and a turbomolecular pump. KBr windows were used to allow a spectrometer beam entry.

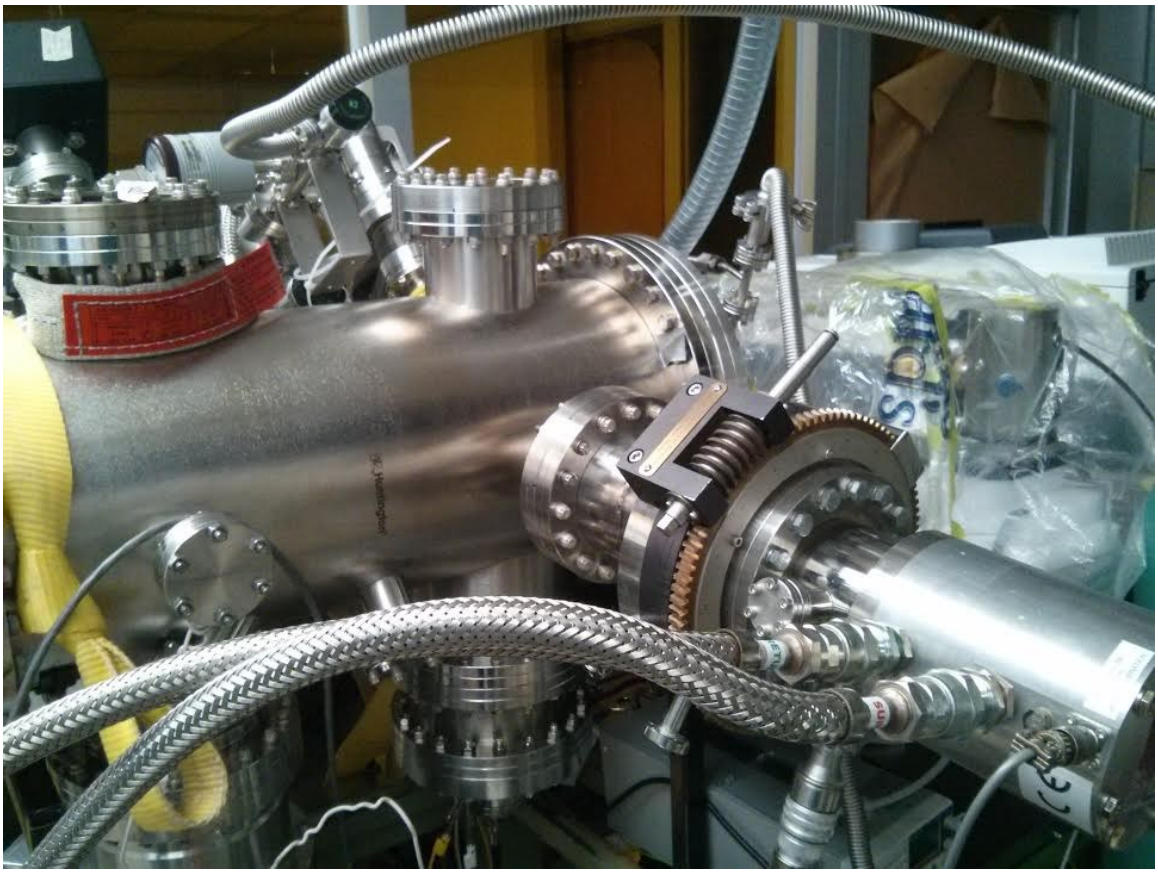

Figure 23. Vacuum chamber used for testing of high temperature electron beam evaporator.

A cryostat manufactured by ARS Cryo was used, capable of temperatures as low as 6 Kelvin. A polished, nickel-plated surface was mounted to the cold head for use as a matrix isolation substrate. The reverse side of the substrate held clips for the attachment of wafers to test deposition rates by growing thin films. The cryostat was mounted on a rotatable flange such that the head could be turned to face the windows, the gas nozzle, or the evaporator, with a position at 45 degrees to the evaporator and gas nozzle being used for the majority of depositions. The cryostat's orientation was horizontal to allow the evaporator to sit vertically. Argon gas was used to generate ice matrices to isolate evaporant molecules. A custom-made gas nozzle with numerous holes along one side was used to promote uniform ice growth. The gas manifold was backfilled with an

atmosphere of argon, with the rate of entry into the chamber controlled with a leak valve. A residual gas analyzer (RGA) manufactured by Extorr Inc was used to determine the partial pressures of gases present in the vacuum chamber. The RGA consists of an RF quadrupole used to permit entry to ions of specific masses only; scanning through the masses with time can be used to track the changing pressures as gases evolve from the sample. The Vacuum Plus software shipped with the RGA is capable of controlling the instrument and displaying the current pressures, but does not log data over time, so software was written in C and MATLAB to read partial pressures from Vacuum Plus and write to a Microsoft Excel readable file. This allowed for the measurement of partial pressures of various molecules expected, such as H2O and SiO, over extended periods of time. An ion gauge was used to monitor the total pressure of the chamber during trials. A window above the evaporator allowed for easy temperature measurement with an infrared thermometer. The thermometer was later moved to a side window and mounted on a tripod to make adjusting the reticle easier. A possible improvement to this design, containing all of the same elements, is shown in Figure 24. The trial system's optical design was fairly straight-forward. The spectrometer used was a Nicolet 6700 Fourier transform infrared spectrometer. An infrared beam generated by the spectrometer passed through a window on the chamber and struck the cryogenic substrate surface, passing through the sample and inert host matrix; it would then reflect out a second window and onto an optical table where an off-axis parabolic mirror was used to focus it into an MCT-A mid-infrared detector (Mercury-Cadmium-Telluride, 12500-400 cm^{-1} range).

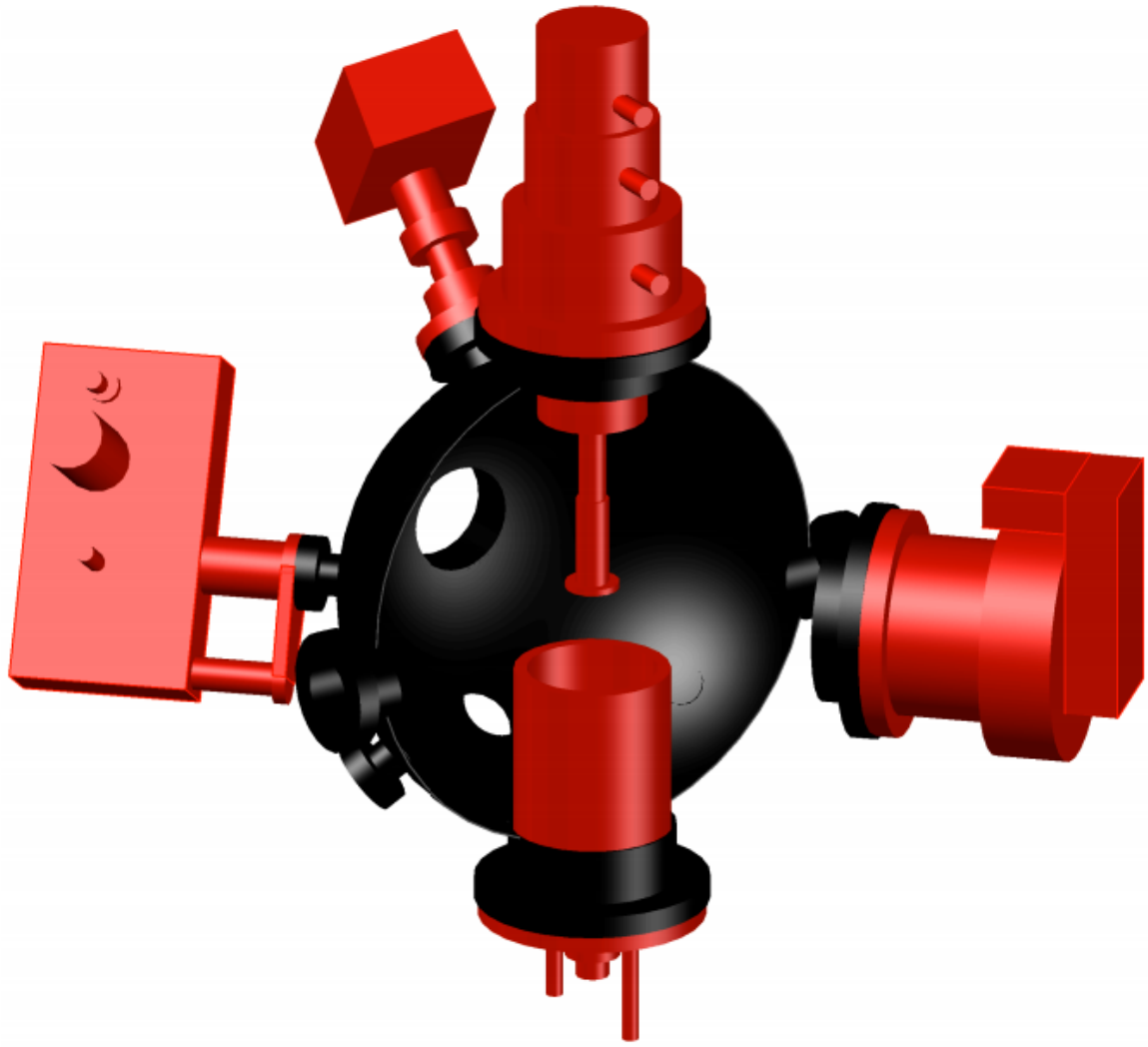

Figure 24. A proposed future chamber design which simplifies in-situ spectroscopy. Clockwise from left: matrix gas manifold, residual gas analyzer, cryogenic substrate, turbomolecular pump, high temperature electron beam evaporator.

The majority of the beam path lay outside of the chamber, necessitating the use of a purge gas system to remove water, carbon dioxide, and other infrared active atmospheric gases (Fig. 25).

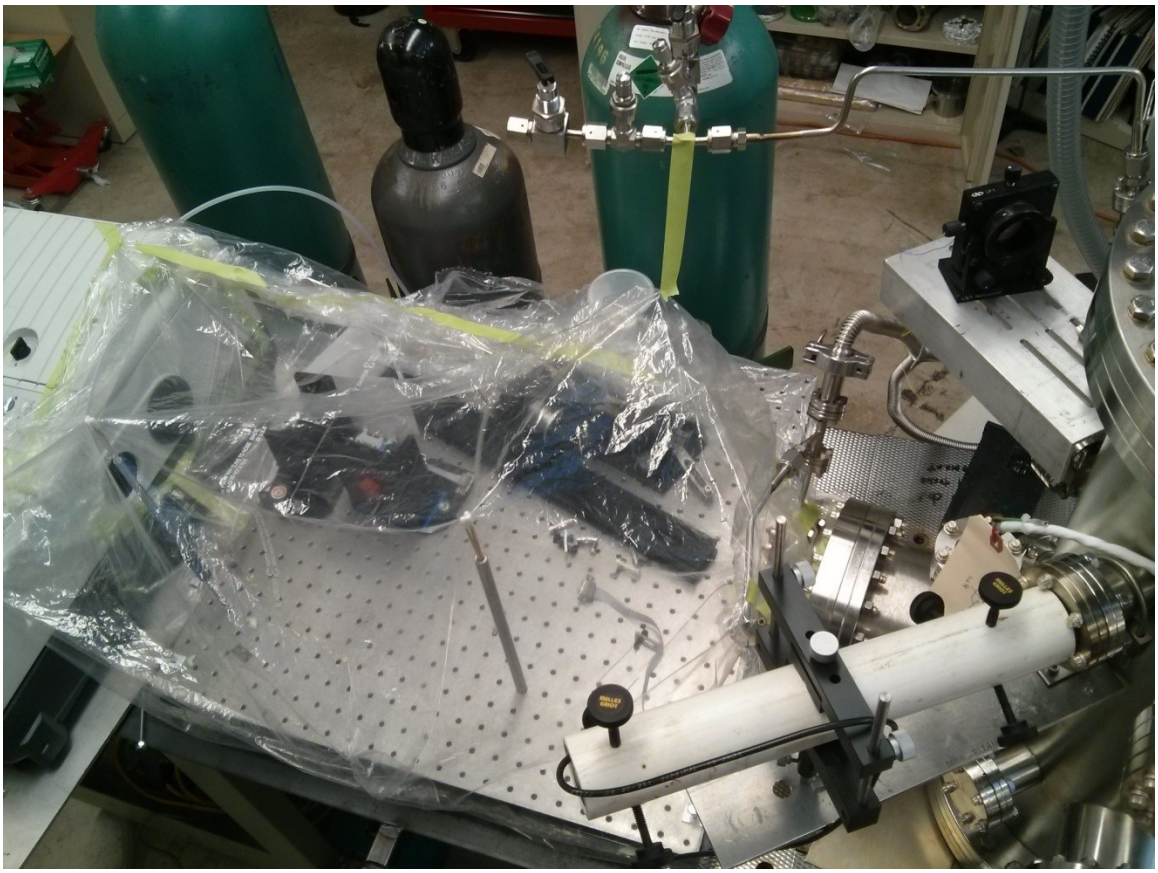

Figure 25. Optical table with purge gas system. The spectrometer is visible to the left and the effusion chamber to the right side of the photograph.

High Temperature Evaporation of Water

Fegley et al have postulated that hot super-Earths might have atmospheres containing up to 50% steam. It therefore becomes desirable to be able to evaporate water along with other theoretical atmospheric constituents in a Knudsen cell. However, as water has a very low boiling point and high vapor pressure, it would ordinarily be impossible to study water equilibrated with silicates at the temperatures at which silicates begin to form significant quantities of vapor. There are several methods by which one might be able to conduct this study. One would be to pipe in water during the evaporation process (Fig. 26). However, as it would be impossible to add water directly

into the Knudsen cell during effusion, a second cell would need to be used, surrounding the first (Fig. 27). This brings with it several difficulties, most notably that an electron beam method cannot be used to heat an inner and an outer crucible, merely the outer one, and that the outer crucible would not be in true equilibrium with the inner (Copland and Jacobson 2010).

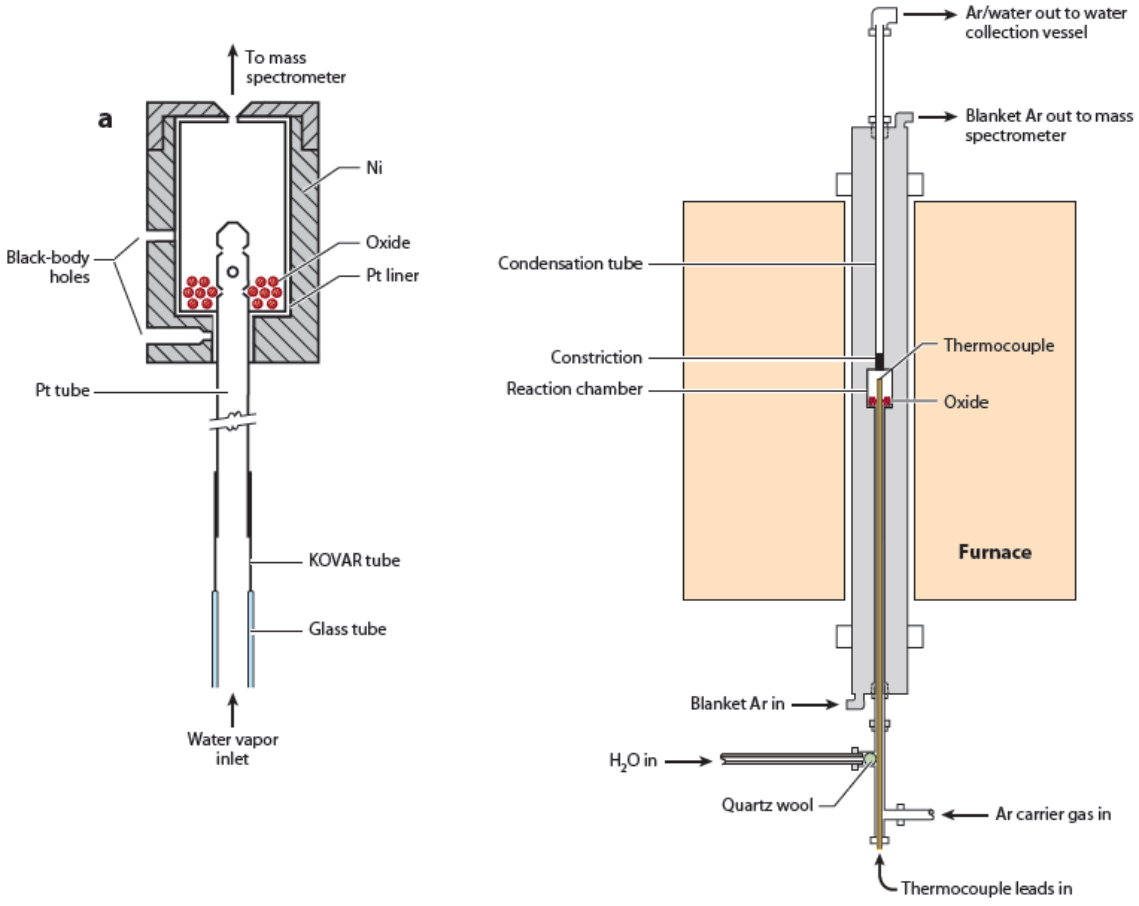

Figure 26. Techniques for adding water to an equilibrated atmosphere (Meschter et al 2013)

Figure 27. Double crucible used by N. Jacobson to study interactions with water vapor.

Another method, examined over the course of this study, would be to use sample materials that can incorporate water directly into the environment. One example is inclusions: rock materials with pockets of water bound in their structure. In this situation, water would only be able to escape once the material surrounding it begins to melt, so water evaporation is seen only above the melting point of the material or other high temperature at which phase transitions occur. This makes it possible to study evaporants including water at temperatures greatly in excess of 100 ºC. Several silicate minerals known to contain water were tested for this property. A simple resistive heater was used to raise material temperatures past their melting points and residual gas analysis tracked the evolution of gases with temperature. Temperatures were verified using Ircon Modline V and Ultimax infrared thermometers.

RESULTS

Evaporator

After construction, the thermionic emission characteristics of the device were measured. Crucible temperatures were monitored for varying currents and voltages. It was verified that the same temperature could be achieved for the same power read on the anode supply; raising the emission current and lowering the bias voltage or raising the voltage and lowering the current but maintaining the same product yielded the same temperature, with an exception at low emission current but high filament current that will be detailed later. The evaporator is shown in Figures 28 and 29.

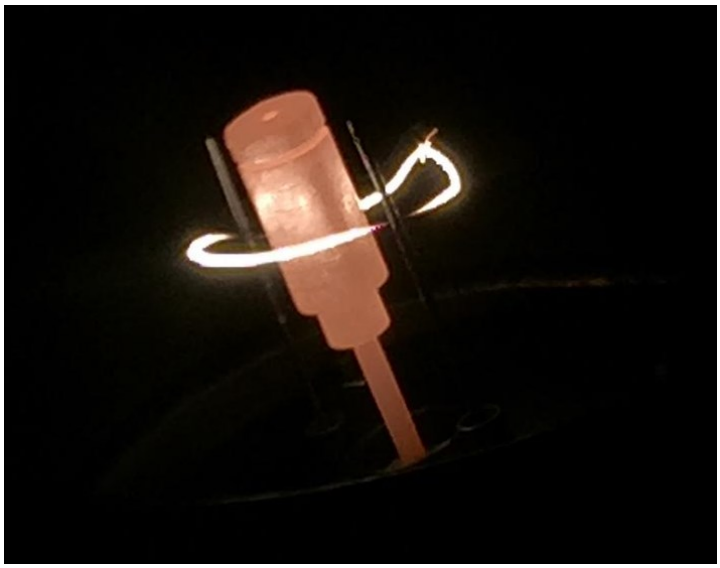

Figure 28. Evaporation crucible heated by thoriated tungsten filament to approximately 1000 degrees Celsius.

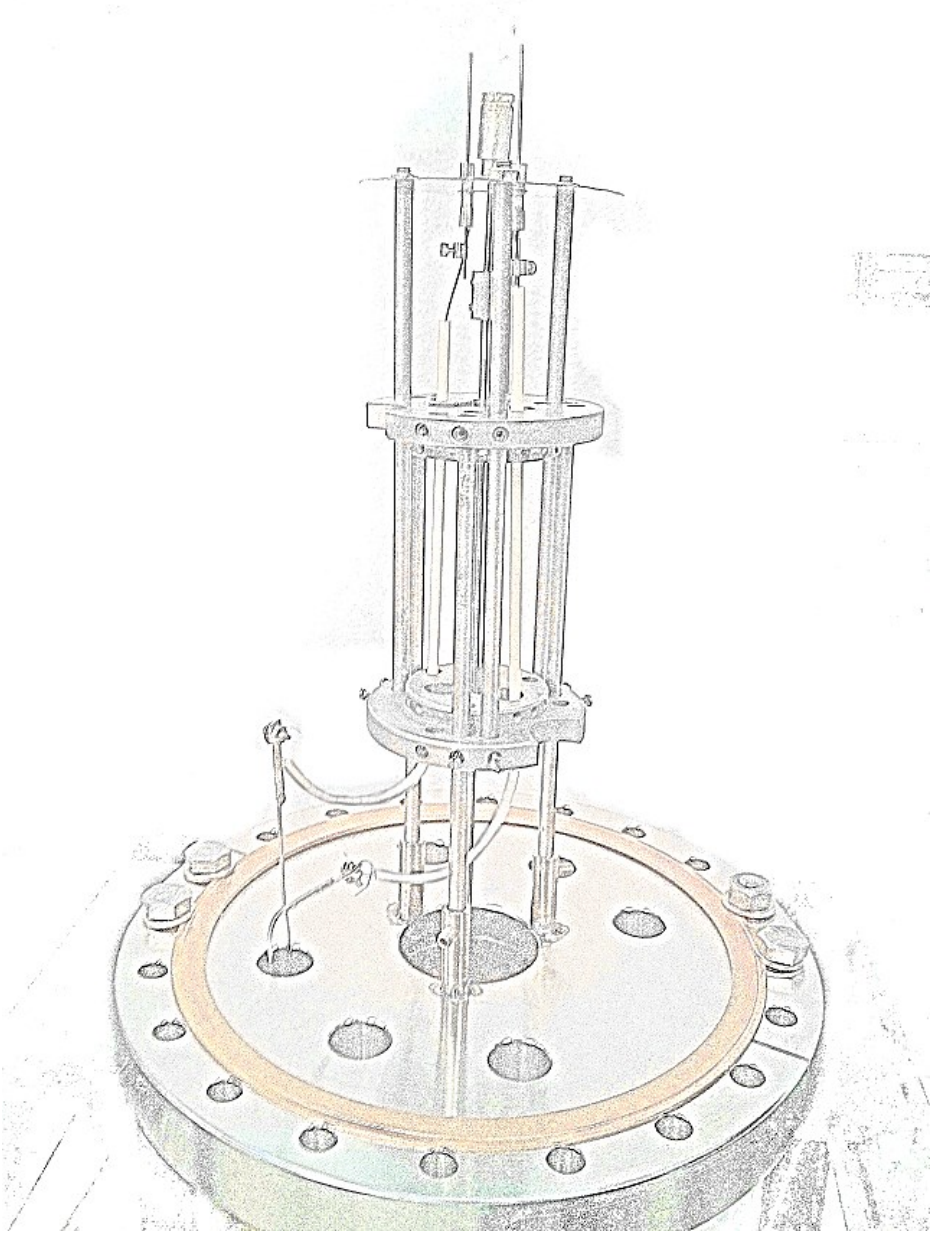

Figure 29. High temperature electron beam evaporator constructed by the author.

As Figure 30 illustrates, when the cathode temperature remains constant, increasing anode voltage will cause emission current to increase dramatically over a short voltage range, called the space charge limited region. Emission current in this region approximately obeys the Child-Langmuir law for thermionic emission:

$$J = \frac{K\, V_{acc}{}^{3/2}}{r^2} \tag{6}$$

Where J is the current density, V_{acc} is the potential applied to the anode, r is the distance between the anode and the cathode, and K is a constant approximately equal to 0.002334 mA $V^{-3/2}$. After a certain voltage, space-charge effects dominate and the emission current levels off, called the temperature limited region. To be precise, the emission current for a saturated filament follows Richardson's law:

$$J = A_0 T^2 e^{-\phi/k_B T} \tag{7}$$

Where T is the cathode temperature, ϕ is the work function of the cathode material, k_B is Boltzmann's constant, and A_0 is Richardson's constant (Dodd 1971).

To raise the emission of a saturated filament it is necessary to raise the temperature (in effect, raising the filament current). In other words, fine control with the anode supply is possible in the lower voltage region only. It is preferable to control the evaporator's power through the anode supply because this allows the filament temperature to remain constant. However, to achieve high power it is necessary to use the upper end of the voltage or to operate at a very high cathode temperature, which could damage filaments (particularly if thoriated tungsten is being used, as it becomes ductile and sags after prolonged high heating) and which contributes to radiative heating of the anode and of the rest of the evaporator. In that sense, the ideal operating parameters for preserving durability of the evaporator are as far into the saturation region as possible, using cathode temperature to control emission current.

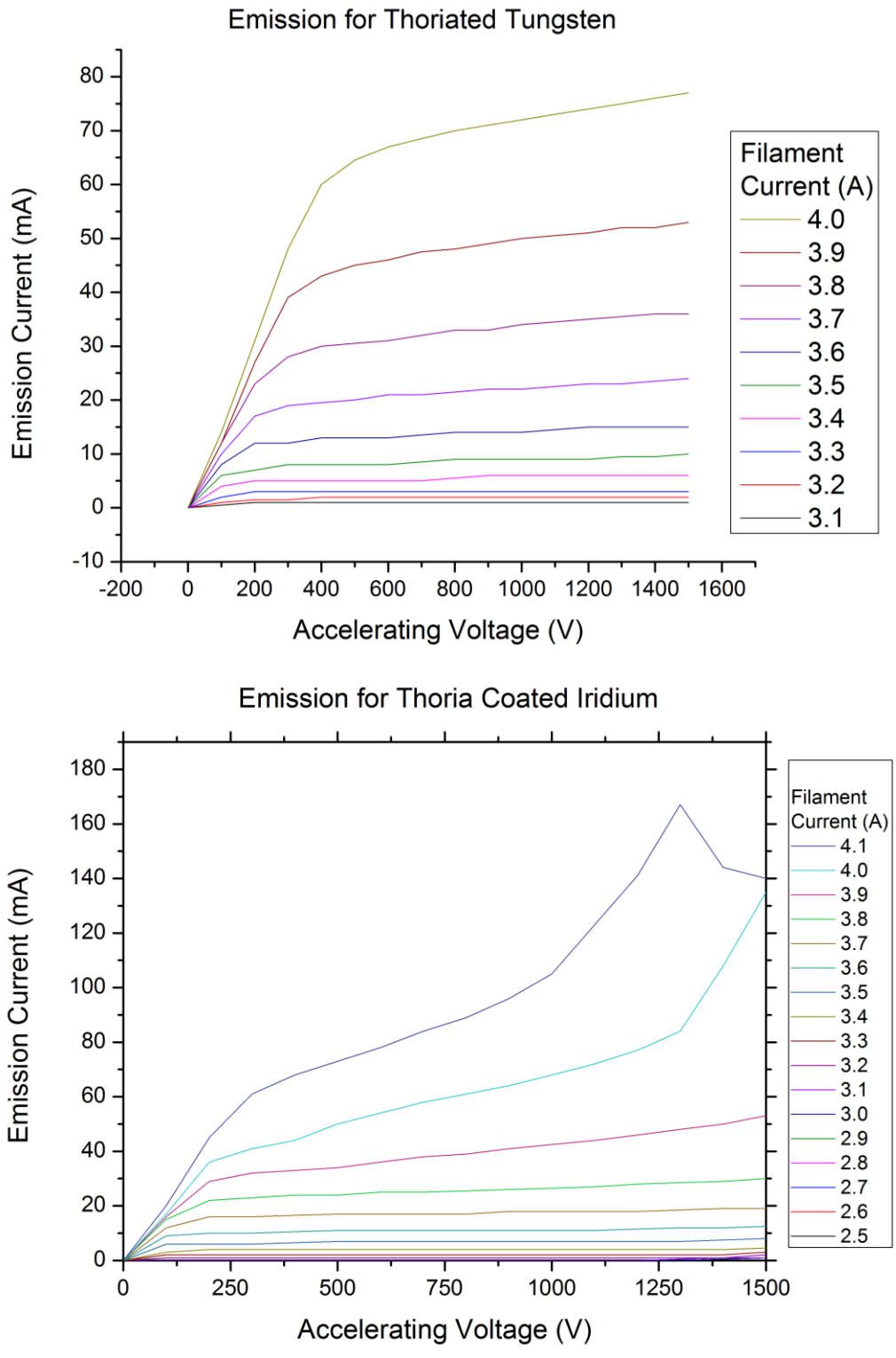

Figure 30. Emission characteristics for thoriated tungsten and thoria coated iridium filaments. Note the drastic increase in emission above 1 kV for 4.0 and 4.1 A filament current, thought to be caused by positive feedback between the cathode and the anode which can radiatively heat one another.

Although the evaporator was intended to heat only through electron bombardment, in practice heating was discovered to come from two sources: the electron beam and radiative heating from the approximately 1350 C cathode less than a centimeter from the anode. Radiative heating dominates at low heating powers, but is negligible at high power once the anode temperature far exceeds the cathode temperature. This can be seen on the temperature-power graph (Fig. 31) where low powers have a spread in temperature caused by the filament temperature while high powers overlap one another closely.

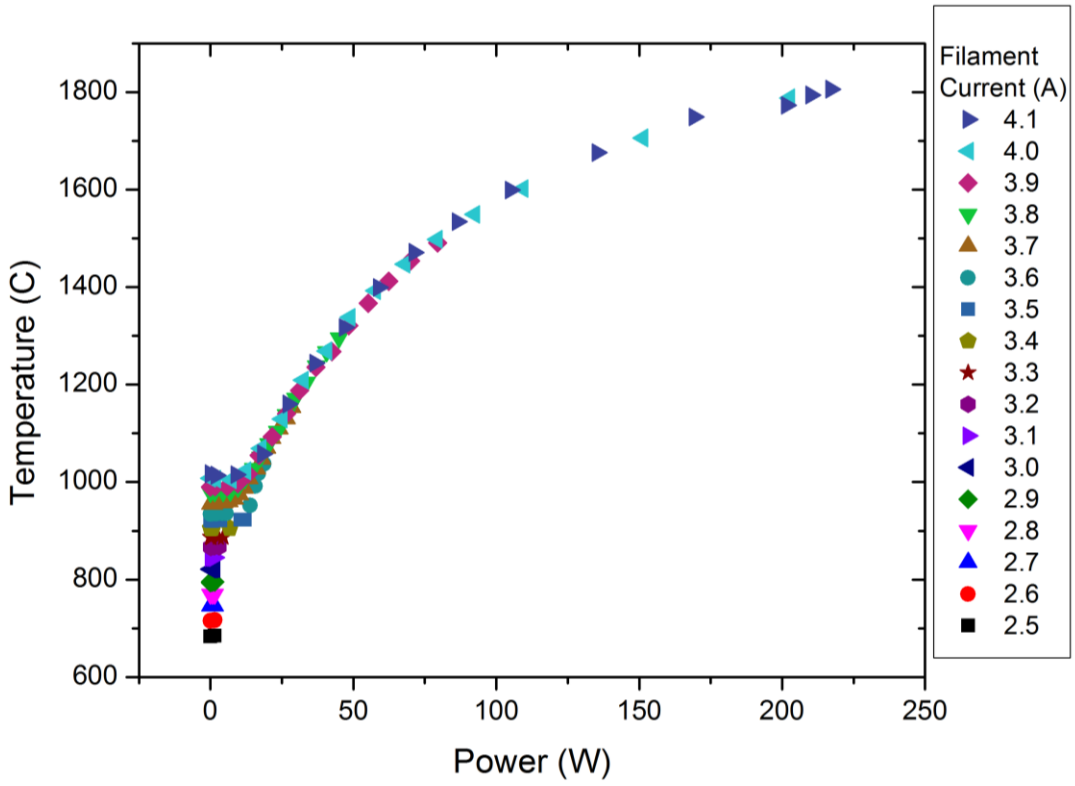

Figure 31. Crucible temperature plotted with increasing heating power $P = I_{emis.} \times V_{acc.}$ for varying filament currents for the thoria coated iridium cathode. Note the near-overlap of points in the high power region (>25 W).

This effect means we can achieve a given power through any combination of accelerating voltage and emission current whose product equal that power (for high

powers). A closer look at crucible temperatures at low accelerating voltages demonstrates that the spread is due to radiative heating effects, as shown in Figure 32.

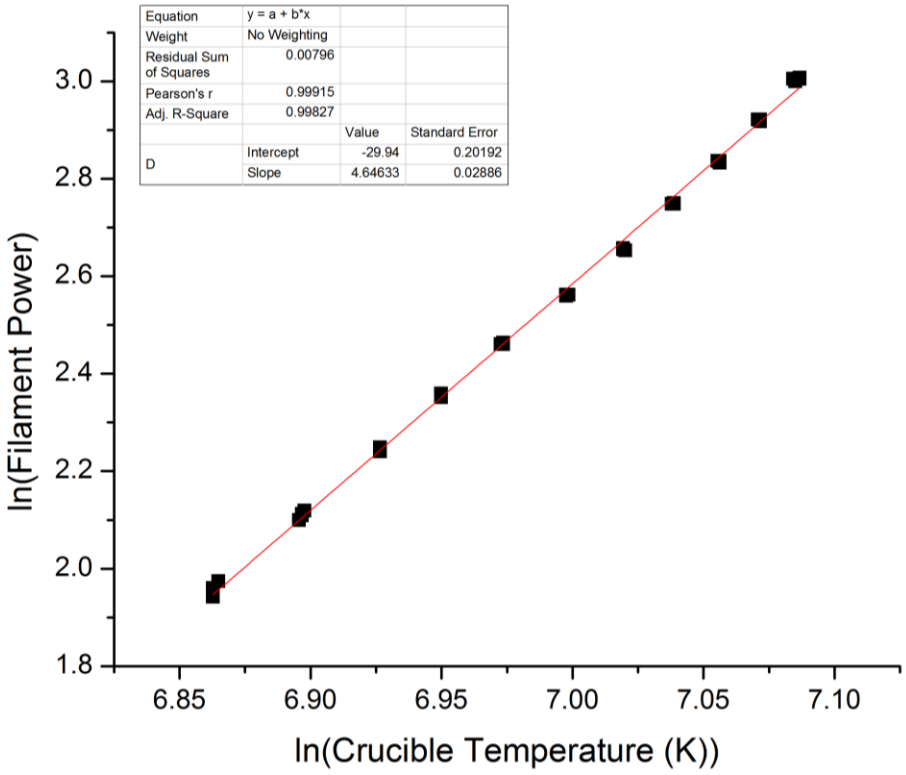

Figure 32. Log-log plot of crucible temperatures for the lower power region plotted with filament power $P = I_{fil.} \times V_{fil.}$ for varying filament currents for the thoria coated iridium cathode. Data were fitted to the curve $P = CT^{4.6}$ using Origin, demonstrating the radiative heating component.

An interesting side-effect of radiative heating in the electron beam evaporator is that it works both ways: once the anode is hotter than the cathode, it actually heats the cathode radiatively instead. This can be measured by tracking the voltage and current on the cathode power supply as the filament's resistivity changes with increasing anode temperatures. When the cathode supply is operated under constant current, this can lead to a positive feedback loop where high anode temperatures heat the cathode, stimulating

greater thermionic emission and raising the anode temperature further, which in turn raises the cathode temperature. At high anode temperatures this effect causes a rapid increase in emission that could lead to exceeding the power limits on either power supply if left unchecked. Operating the cathode supply in constant voltage mode causes a negative feedback loop instead, where emission gradually drops. This behavior is due to the temperature dependence of resistivity in materials: metals, which are used for our filament and crucible materials, increase in resistivity with increasing temperatures. If for whatever reason insulating materials were used instead, this effect might occur in reverse. At present, this means that the instrument must be monitored and adjusted as necessary by a human operator. In the future, however, this issue could be rectified by either using a power supply capable of constant power mode operation or by controlling the instruments using a computer program running a PID (proportional, integral, derivative) loop. A PID loop is an algorithm which controls feedback loops by approaching a setpoint through a combination of the current difference (proportional), the past difference (integral), and the current rate of change (derivative). The three values have weights which are determined during calibration.

Effusion rates for an electron beam evaporator depend on the temperature achieved and the vapor pressure of the sample material at that temperature. They are also constrained by Knudsen cell orifice size and any apertures used in the instrument. Measurements of flux rates can be made through several methods: use of a quartz crystal microbalance, studying diffraction/interference intensity using a laser, and measuring the thickness of thin films grown onto a substrate with a microscope or a profilometer. For

this study, a DekTak profilometer was used to analyze the thickness of a thin film grown onto GaAs wafer substrates (Fig. 33, Fig. 34).

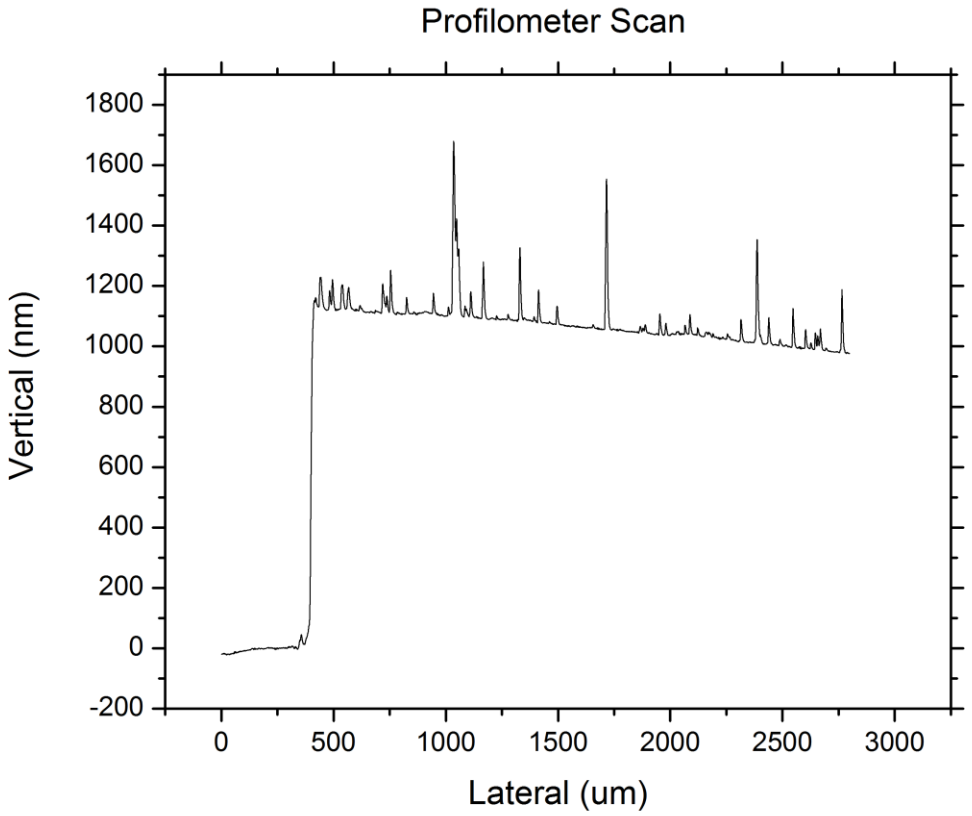

Figure 33. Thickness measurement of SiO thin film grown at 1600 ºC for 24 hours with a 1 mm diameter orifice and no shutter or aperture demonstrates 1.126 um growth, or 46.91 nm/hr.

For example, 47 nm/hr deposition of SiO on a 1 cm by 1 cm substrate is a rate of 4.64×10^{13} atoms per second. An ideal co-deposition rate for argon would be 4.64×10^{16} atoms per second, or 10^{-5} torr. Rates this high, resulting in rapid growth of ice, can result in low spectroscopic signal, so reducing the rate of argon deposition can improve the overall results. For this reason, controlling the evaporation rate using a shutter or smaller aperture is crucial at higher temperatures. In addition, high chamber pressures negatively

affect evaporator performance, particularly causing arcing and filament burnout, although this can be mitigated somewhat through the geometry of argon deposition and restricting the path to the evaporator with a cooling jacket.

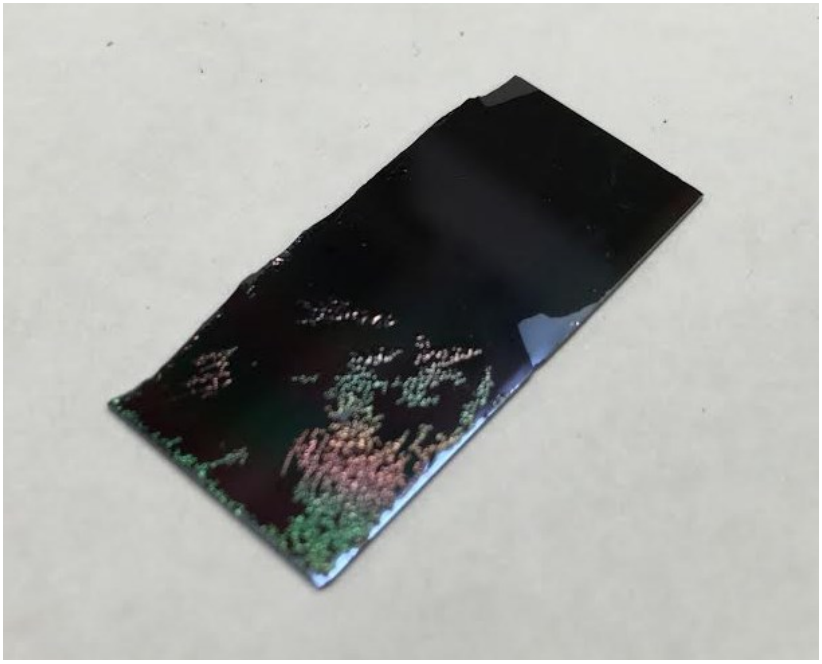

Figure 34. Gallium arsenide wafer with SiO thin film.

Water Inclusion at High Temperatures

Several silicates were studied to determine the rate at which water outgassed at high temperatures, including opal and milky quartz. Residual gas analysis was used to probe partial pressures for SiO_2, SiO, H_2O, and their constituents. Opal, which consists of up to 21% water bound in its structure, was discovered to lose all of its water at 700 ºC (Fig. 35). Milky quartz, which is an SiO_2 crystal containing microscopic water inclusions, was found to lose the majority of its water at 800 ºC (Fig. 36). Reheating of samples after a cooldown period discovered no further water losses.

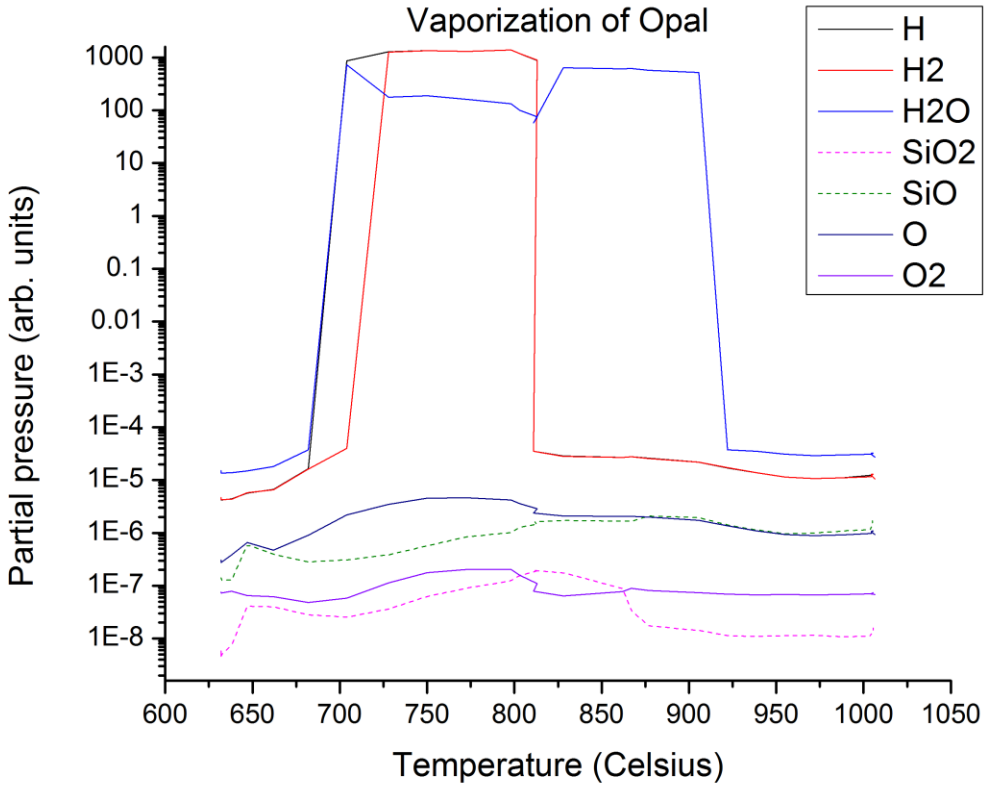

Figure 35. Residual gas analysis of opal during heating. Water is demonstrated to leave the crystal at 700 ºC.

Because water's vapor pressure is many orders of magnitude greater than that of quartz or opal, it is sufficient to retain only a small percentage of the overall water at the desired high temperatures. For example, to test the hypothesis that a silicate exoplanet's atmosphere might contain up to 50% water vapor, water pressure within the evaporation crucible would need to equal that of that of the silicate vapors. If the planet had a day side surface temperature of 1500 ºC, its primary atmospheric constituent, SiO, would have a vapor pressure on the order of 20 torr, while water will exist entirely as a vapor. To generate 20 torr of water vapor within the evaporation crucible thus requires a very minute quantity of residual water (on the order of a micromole per mole of silicate).

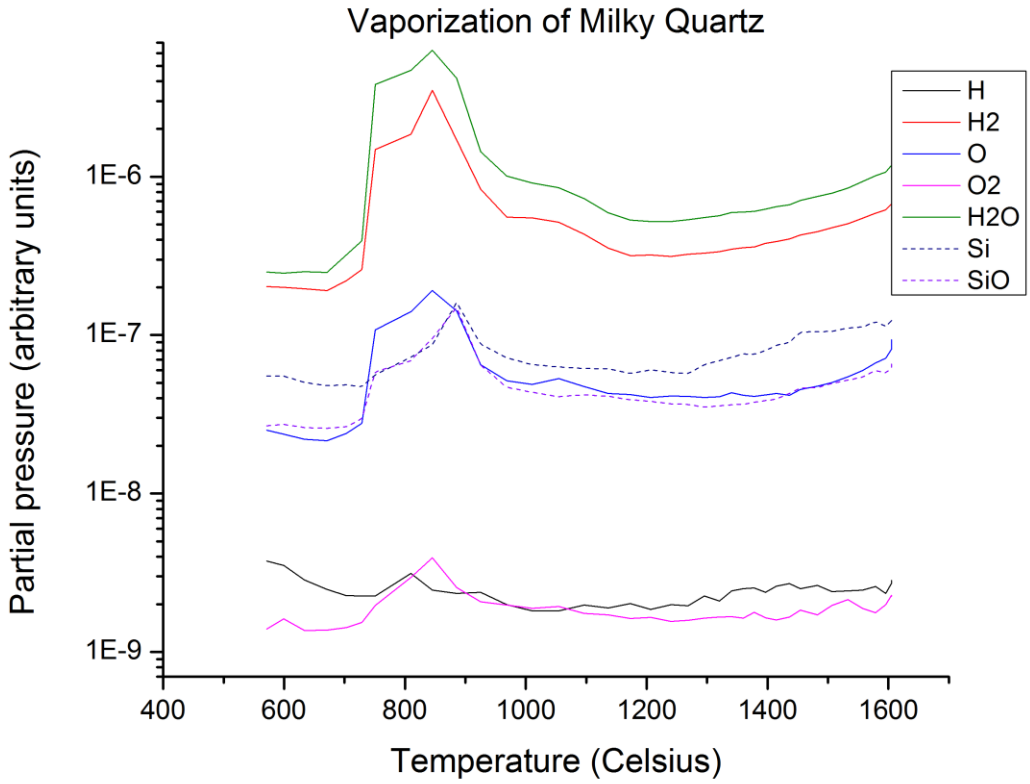

Figure 36. Residual gas analysis of milky quartz during heating. Water and its constituents are liberated at 800 ºC, during a possible phase transition; quartz itself, along with additional water, begins to enter the vapor phase at 1250 ºC.

High Temperature Measurement of SiO_2

The ultimate goal of this project is to collect data on evaporated silicates and other compounds. To that end, silicon dioxide was evaporated in a Knudsen cell at 1600 ºC using electron beam evaporation and co-deposited onto a 40 K substrate with argon ice. Spectral measurements were made of the 400-7000 cm^{-1} mid-infrared region using a Nicolet 6700 FTIR spectrometer. Peaks corresponding to a number of silicates have been identified after data analysis in MATLAB (Appendix B), as shown in Figure 37. Integration of individual peaks can be used to determine constituent ratios; see Figure 38.

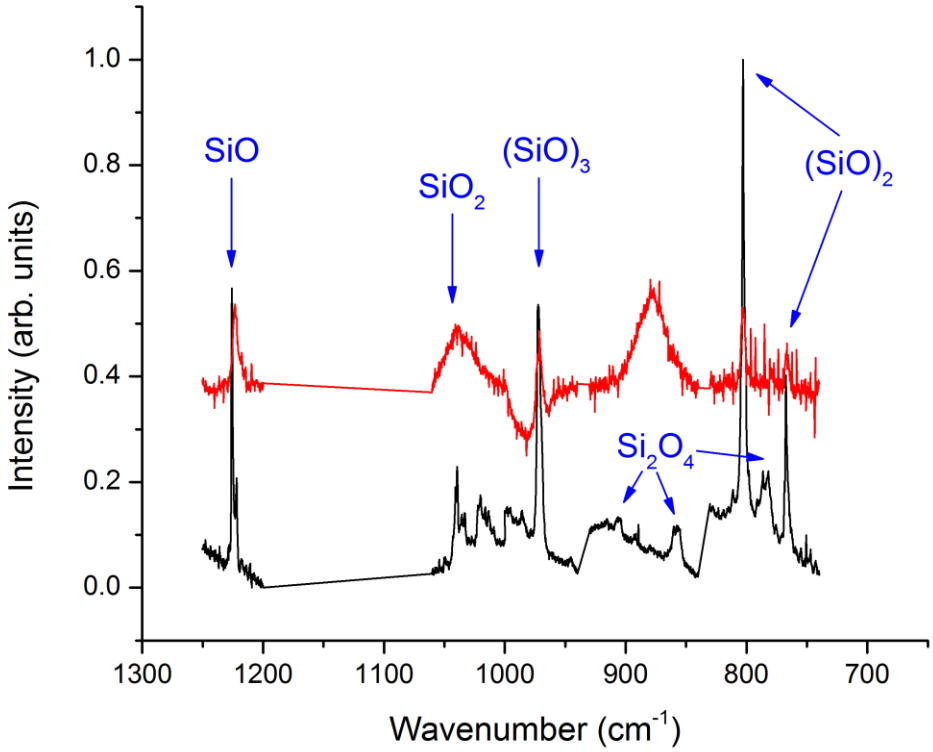

Figure 37. Absorption spectrum of equilibrated vapor phase of SiO_2 powder co-deposited with 40 K Ar ice at 1400 ºC (black) and 1600 ºC (red). Low signal for the 1600 ºC run makes clean background subtraction difficult but peak overlaps can be seen for SiO, SiO_2, and the dimer and trimer forms of SiO.

An approximation of the column density of the molecular species present can be made by integrating the area of the peaks in the infrared spectrum (Hedelund et al 1972). By using transition probabilities provided by Geballe et al (1979), we obtain a column density of 5×10^{18} per square centimeter. This value can also be calculated from the thickness of the thin film grown in the absence of argon, from the density of SiO, which results in 3.303×10^{18}. From this value we can approximate the total flux leaving the crucible aperture.

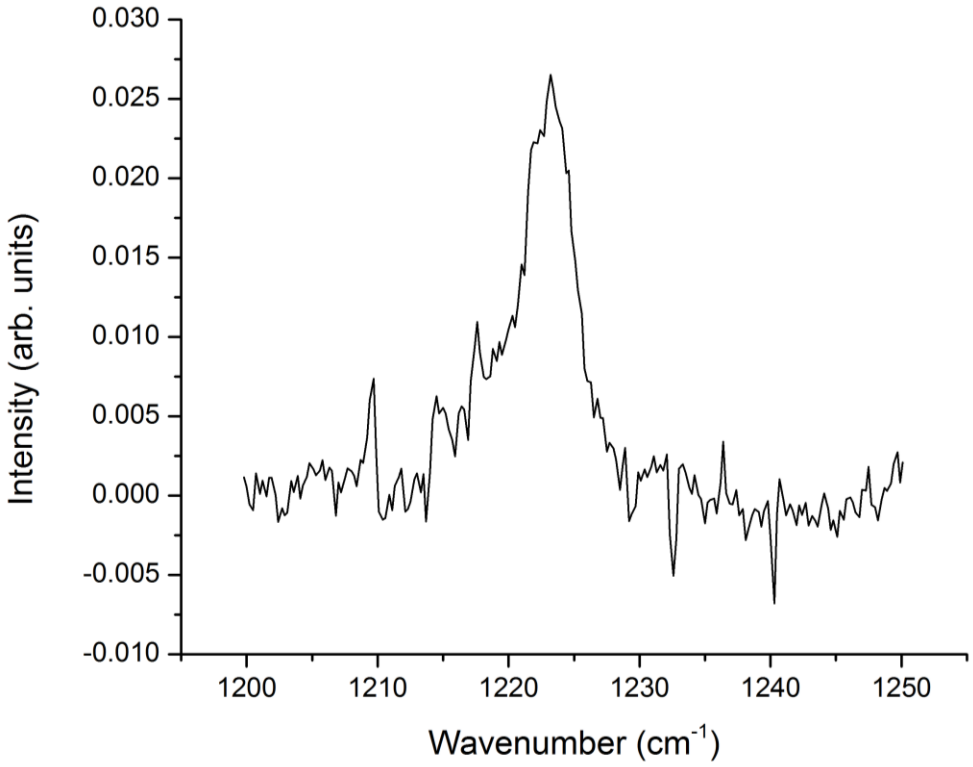

Figure 38. 1223 cm^{-1} Si=O stretch corresponding to SiO monomer after background subtraction from the 1600 ºC SiO_2 deposition sample shown in Figure 37. Integration of the peak provides a peak area of 0.16469143675.

The relationship between the peak value and the total flux is essentially given by a cosine distribution; we calculate a total flux of 5.83×10^{15} SiO molecules per second from the thin film growth rate. We can then obtain the partial pressure of SiO evaporated from SiO_2 at 1600 ºC from the Hertz-Knudsen equation (Eqn 2), assuming an ideal Clausing factor of 1 and given the aperture diameter of 1 mm, to be 0.8093 Pa. Evaporation studies of SiO_2 show a vapor pressure on the order of 1 Pa (Iosilevskiy 2014), although it should be noted that other evaporation products (in particular O and O_2, which are not present in the thin film or infrared spectrum) make up a substantial portion of the vapor released by SiO2 so the calculated 0.8 Pa can be assumed to be below the total value.

Spectral Modeling for Astrophysical Interest

After generating spectra in the lab, it is necessary to format them in such a way that they can be compared to the results an astronomer might collect. Recall that exoplanets, particularly smaller ones like hot super-Earths, are far less intense than their host stars, making direct spectroscopic measurements infeasible. Instead, astronomers rely on binning techniques using filters, an example of which can be seen in Figure 13. In order to relate our reference spectra to such results, they must be processed in such a way that photometric intensities are outputted for a given set of filters. Before that, however, there is a greater challenge: creating an atmospheric spectrum from an absorption spectrum. A reference spectrum, as seen in Figure 37, consists of peaks which have had the background subtracted. The spectrum an astronomer might observe, with sufficiently advanced instrumentation, would contain a background based upon the source of the light. The first task is therefore to construct a background.

There are two primary sources of the light we see when we look at an exoplanet: the star and the planet itself. The star's light approximates a black body at the effective temperature of the star, with the maximum intensity corresponding to wavelengths in the blue region for a hotter star down to the red region for a cooler star, while light from the planet approximates a much cooler black body whose maximum is in the infrared. We model these sources using Planck's law for blackbody radiation:

$$B(\lambda, T) = \frac{2hc^2}{\lambda^5(e^{hc/\lambda k_B T} - 1)} \tag{8}$$

Where B is the intensity of the light at a given wavelength and T is the temperature of the black body, shown in Figure 39. We can add absorption lines to this model as necessary following Equation 4 in the theory section.

As the planet is so much smaller and cooler than the star, the majority of the light will be coming from the star. All of the light emitted by the planet passes through its atmosphere, causing it to contain absorption lines; only a fraction of the light from the star is reflected off the planet, so the majority of it does not contain absorption lines. The ratio of light which contains absorption lines to light which does not will control the depth of the lines and the extent to which the planet's spectrum differs from that of the star. As the planet orbits the star, this ratio is constantly changing; this makes some phases of the planet's orbit more desirable than others for observation.

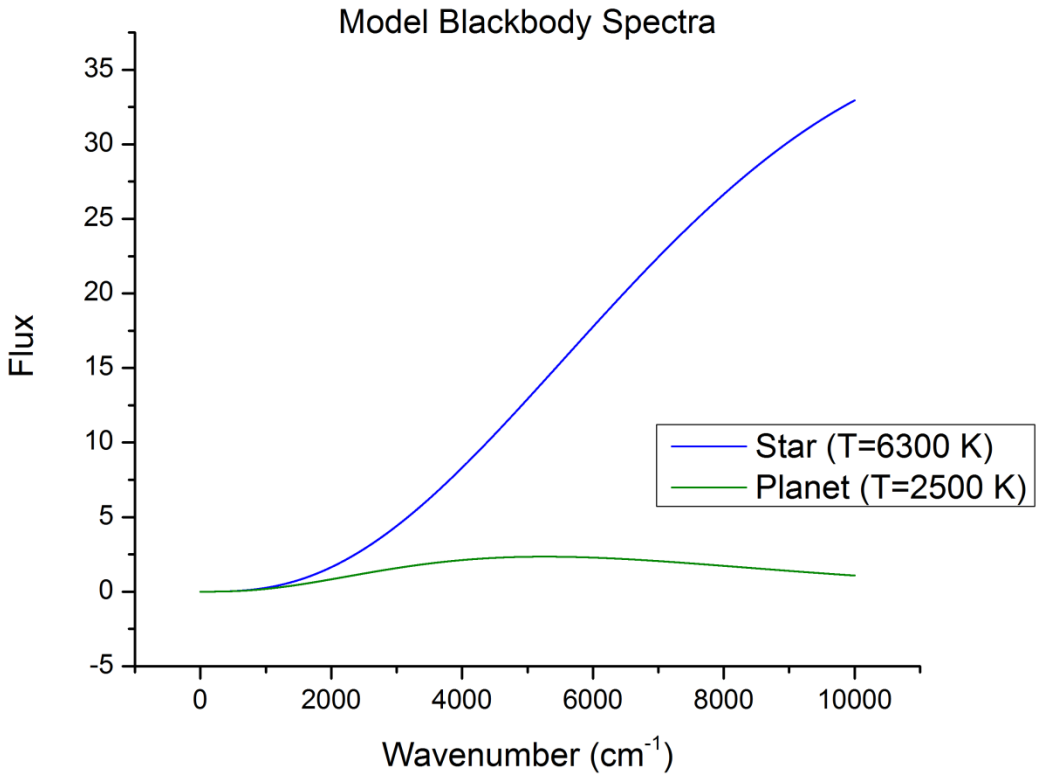

Figure 39. Blackbody spectra for a star (blue) and a hot nearby planet with a surface temperature of 2500 K (green).

To model this ratio as it changes over the course of the planet's orbit, we must consider the geometry of the system as seen from Earth (a simple representation can be

seen in Figure 40). There are three basic cases. The first and most trivial is when the planet is eclipsed by the star. In this case, the star's contribution relative to total light intensity will be unity and the planet's will be zero. The next case is when the planet transits in front of the star. In this case, again, the planet's reflected contribution is zero with only the blackbody radiation of the planet visible. However, the star's intensity will decrease as a portion of it is obscured by the planet. The star and the planet, as seen by a distant observer can be thought of as two disks which overlap, where the star's disk emits light equally over its entire surface except where overlapped by the planetary disk. The size of the disks is determined by the size of the planet and the size of the star (Armitage 2010). Intensity for a complete overlap is therefore:

$$I = 1 - \left(\frac{R_p}{R_*}\right)^2 \tag{9}$$

Where R_p represents the planet's radius and R_* the star's radius. For a partial occultation with an intersectional area A, intensity becomes:

$$I = 1 - \left(\frac{A}{\pi R_*}\right)^2 \tag{10}$$

The remaining case is when the planet and star do not eclipse one another. In this case, the star's light remains unobscured so its contribution remains unchanged. However, half of the planet's surface is always illuminated by the star, and a fraction of this light will be reflected. The fraction of light reflected by a planet is known as its albedo.

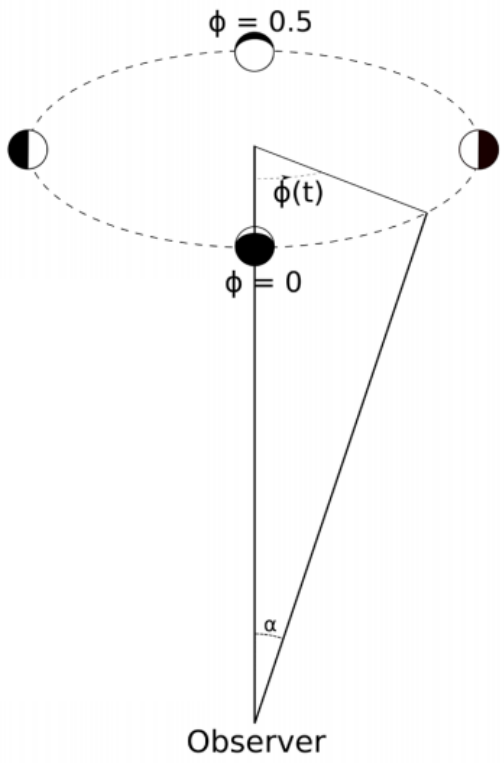

Figure 40. Exoplanet phases as seen by an observer (Martins et al 2013).

The proportion of the day side which is visible from Earth can be represented as a sine function. Combining the albedo α, the visible fraction dependent on the orbital phase ϕ, and the ratio of planet and star sizes and the orbital radius R_o, we get:

$$f = \frac{1}{2}\alpha\left(1 - \cos\left(\phi - \frac{\pi}{2}\right)\right)\left(\frac{R_p}{R_*}\right)\left(\frac{R_o}{R_*}\right) \tag{11}$$

Where f is the fractional contribution of the planet. Putting these cases together, we can generate a simple model for the total light curve with phase, in addition to the ratio of light which has passed through the planetary atmosphere to light which hasn't, shown in Figures 41 and 42.

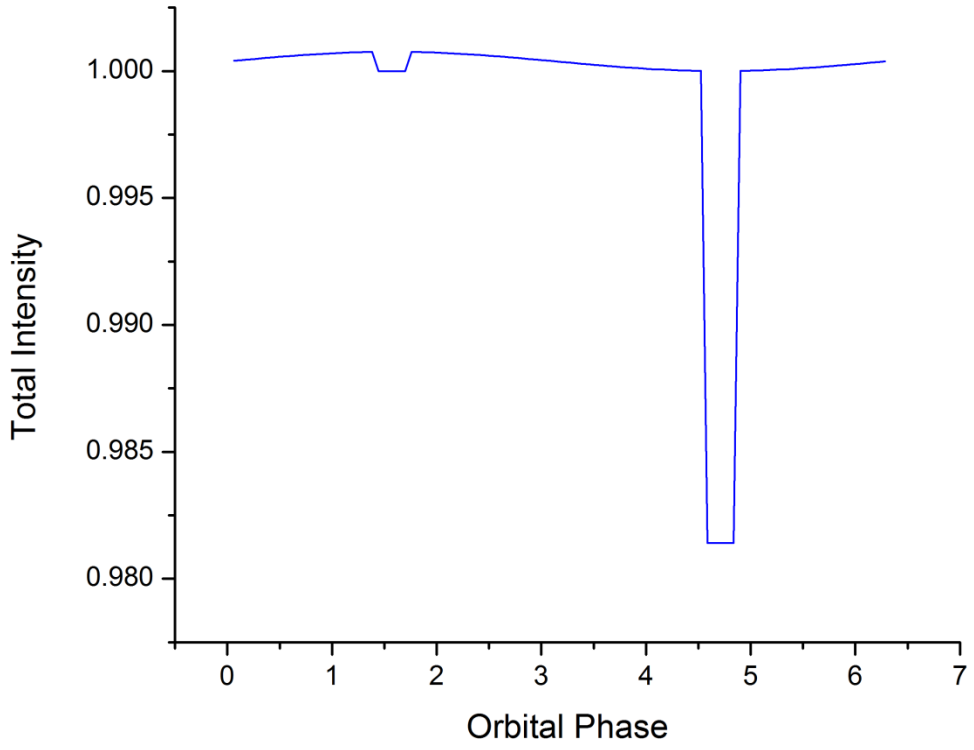

Figure 41. Simulated total intensity for the sun-Earth system.

We now combine the two simulations to create model spectra. This is done by adding the star's spectrum, multiplied by the fractional contribution of the star, and the combined star and planet spectrum containing absorption lines, multiplied by the fractional contribution of the planet. This spectrum must now be converted to a photometric intensity. This is done by convoluting a filter's band pass with the spectrum. By calculating the photometric intensity for each of the filters used by observational astronomers, we can provide photometric references for each of the atmospheric mixes whose reference spectra are generated in the lab using the high temperature effusion system (a MATLAB implementation can be seen in Appendix A).

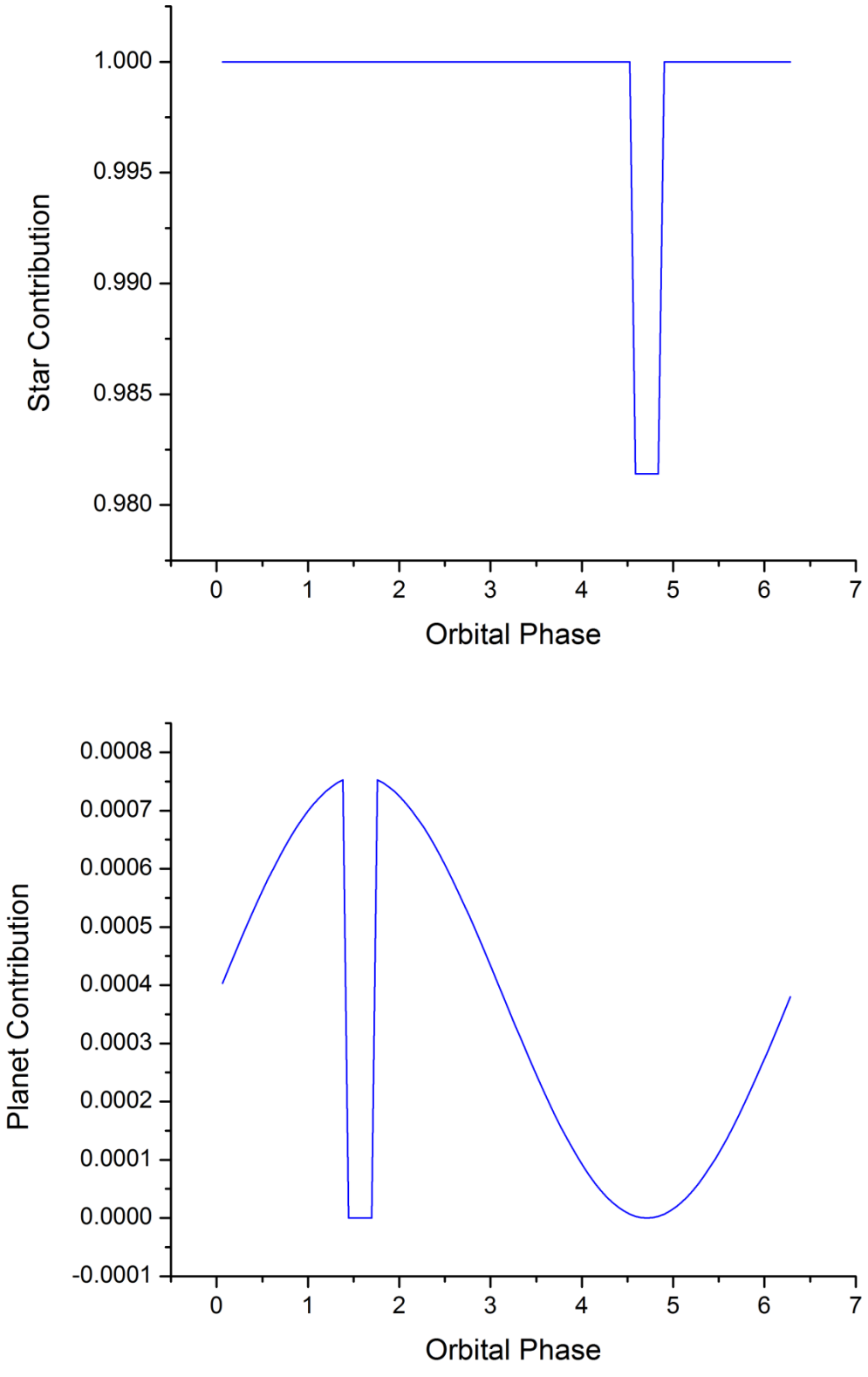

Figure 42. Simulation of fractional contribution of the star (above) and the planet (below) for the sun-Earth system.

There are other implications of this modeling work as well: by generating a model spectrum as astronomers would see it and varying the parameters of our filter set, we can determine which bands would be most useful for verifying composition. A simple example to consider is an exoplanet whose atmosphere is composed entirely of either SiO or CO_2. After generating model spectra for both atmosphere types (Fig. 43), we calculate the photometric intensity of each planet using a filter centered at a point x, where x varies from 500 to 4000 cm^{-1}. The difference in intensities is shown in Figure 44. This demonstrates that if we were to use filters centered at 500 and 1890 cm^{-1}, we see the greatest difference between the two possible compositions.

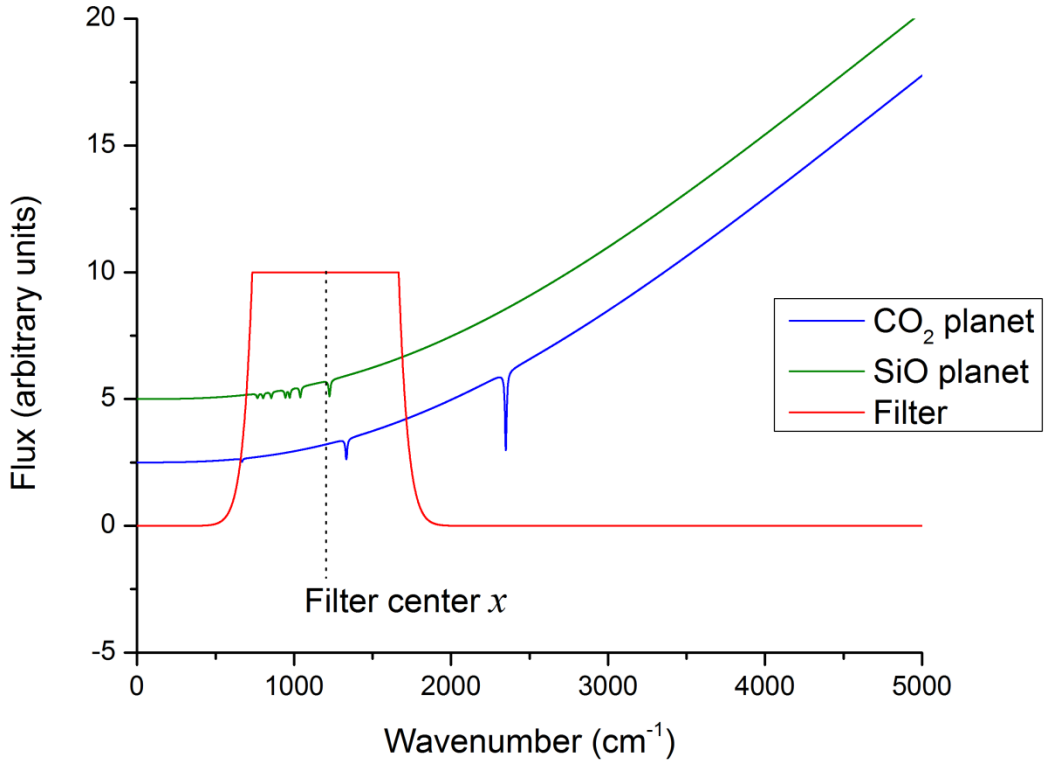

Figure 43. Calculated model spectra for a planet with a CO_2 atmosphere (blue) and SiO atmosphere (green); modeled band-pass filter (red) overlaid centered about x. Constant added to differentiate spectra.

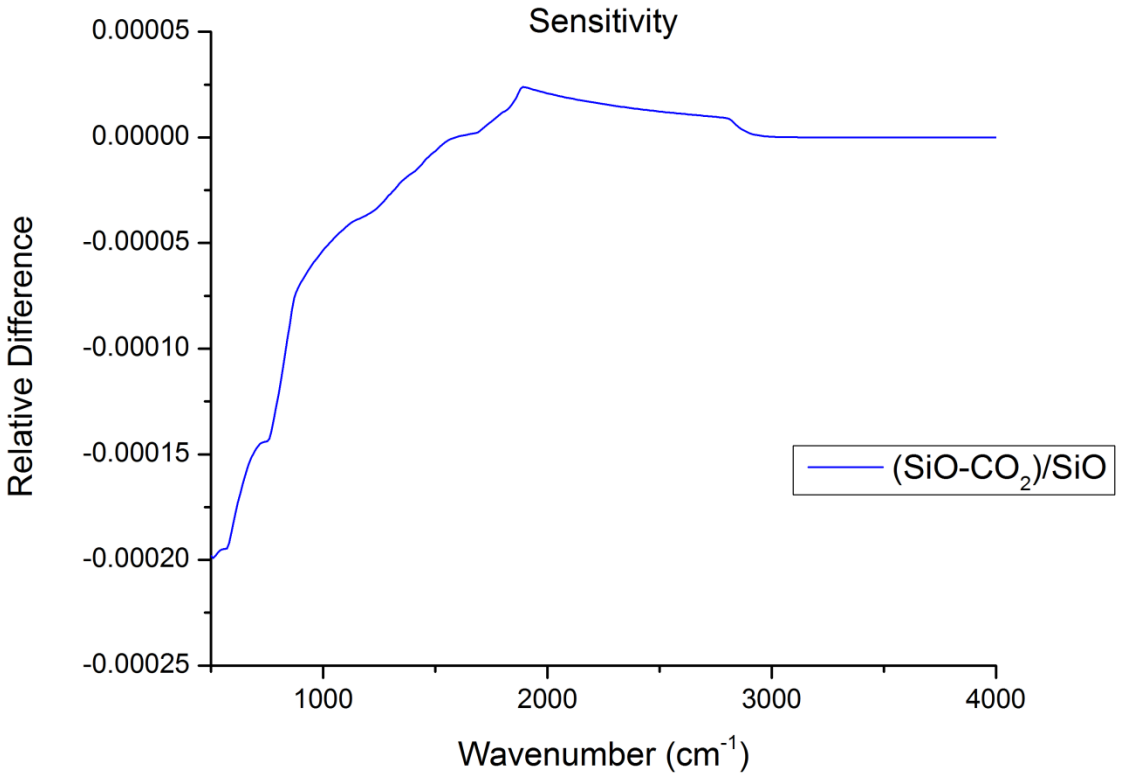

Figure 44. Relative difference between photometric outputs of the two models, plotted with increasing filter midpoint.

Modeling could be further constrained by adjusting the bandwidths of filters used and the number of filters sampled. The ultimate goal of this exercise would be developing an algorithm to intelligently search for the best combinations of filters in order to maximize the variations as measured between all filters. This could be done by maximizing the square of the relative difference between photometric outputs of two or more models through a Monte Carlo technique.

Future Work

Work remains to be done in order to accomplish the goals of this project. Continued testing of the evaporator needs to be carried out in order to determine flux rates for different temperatures and crucible orifice sizes. A shutter needs to be installed with variably sized apertures to allow fine control of deposition rates at set temperatures. The feedback loop issue must be addressed: maintaining temperature stability is a requirement for this project, and the long evaporation times (20+ hours) necessary to collect enough sample at lower temperatures to perform spectroscopy make it impractical to have a student constantly monitoring the instrument. One approach to solving the issue would be to switch to a power supply which can provide constant power instead of constant current/constant voltage. The supply would automatically compensate for any increased or decreased emission due to filament temperatures. Another approach would be to write a program to control the cathode supply based on the outputs of the anode supply, using LabVIEW or similar. The program would detect fluctuations in the emission and adjust the filament temperature accordingly. Operation would follow a PID (proportional-integral-derivative) algorithm.

Another subject of further study is the effect on emission rates of using multiple loop filaments. This was to be studied but had to be postponed due to time constraints. In theory, using additional filaments would bring the emission characteristics more in line with what one would expect for the Child-Langmuir approximation, which uses a cylindrical cathode and centrally located anode which extend to infinity. Even in the simplest case, additional filaments should greatly increase the emission current, allowing lower filament temperatures to provide the same crucible temperature and raising the

maximum temperature achievable using the instrument. The addition of filaments would also help to smooth out any temperature gradients present on the crucible-another potential avenue of study. Isothermal heating is desired, but realistically there probably exists a high temperature zone on the crucible at the same elevation as the filament and a low temperature region at the base of the crucible where it connects to the center rod. This might also be mitigated by using alumina, zirconia, or other high temperature ceramics to stand off the crucible, with only a fine metal wire to connect the anode supply. The thermal properties of high temperature ceramics should prevent as much heat from escaping the system.

Lastly, the overall aim of the project, characterization of reference atmospheric compositions, can be achieved using the high temperature evaporator constructed in this study. This is simply a matter of having crucibles machined, loaded with sample in the desired ratios, and brought to the desired temperature in the vacuum chamber. Some progress on this front has already been accomplished (SiO2 at 1400 and 1600 C).

REFERENCES

Akishin, P. A. 1967, in The Characterization of High Temperature Vapors, ed. J. L. Margrave (Wiley)

Armitage, P. J. 2010, Astrophysics of Planet Formation (Cambridge)

ASTM G173-03(2012), Standard Tables for Reference Solar Spectral Irradiances: Direct Normal and Hemispherical on 37° Tilted Surface, http://rredc.nrel.gov/solar/spectra/am1.5/

Bally, T. 2004, in Reactive Intermediate Chemistry, ed. R. A. Moss et al. (Wiley)

Berman, A. 2014, Total Pressure Measurements in Vacuum Technology (Academic Press)

Carlson, K. D. 1967, in The Characterization of High Temperature Vapors, ed. J. L. Margrave (Wiley)

Copland, E. H., Jacobson, N. S. 2010, NASA Report, NASA/TP-2010-216795

Dodd, J. G. 1971, Am. J. Phys, 39, 1159

Fogtmann-Schulz, A., Hinrup, B., Van Eylen, V., et al. 2014, ApJ, 781, 67

Geballe, T. R., Lacy, J. H., Beck, S. C. 1979, 230, L47

Hannay, N. 2012, Treatise on Solid State Chemistry: Volume 6A (Springer Science & Business Media)

Hedelund, J., Lambert, D. L. 1972, Astrophysical Letters, 11, 71

Howard, A. W., Sanchis-Ojeda, R., Marcy, G. W., et al. 2013, Nature, 503

Iosilevskiy, I., Gryaznov, V., Solov'ev, A. 2014, High Temperatures High Pressures 43.2-3, 227-241

Jacobson, N. S., Copland, E. H., Mehrotra, G. M., et al. 2002, Electrochem. Soc. Proc., 226-232

Léger, A., Grasset, O., Fegley, B., et al. 2011, Icarus, 213, 1

Madhusudhan, N. 2012, ApJ, 758, 21

Martins, J. H. C., Figueira, P., Santos, N. C., Lovis, C. 2013, MNRAS 436, 1215-1224

Meschter, P. J., Opila, E. J., Jacobson, N. S. 2013, Annu. Rev. Mater. Res, 43, 559-588

Miguel, Y., Kaltenegger, L., Fegley, B., Schaefer, L. 2011, ApJL, 742, L19

Miller, M., Armatys, K. 2013, The Open Thermodynamics Journal, 7, 2

Nakayama, A., Niimi, K., Ono, Y., Taketsugu, T. 2012, J. Chem. Phys. 136, 54506

Rouan, D., Deeg, H. J., Demangeon, O., et al. 2011, ApJL, 741, L30

Schaefer, L., Lodders, K., Fegley, B., 2012, ApJ, 755, 41

Shukla, A. K., Banik, S., Dhaka, R. S., et al. 2004, Review of Scientific Instruments, 75, 4467

Smith, B. C. 2011, Fundamentals of Fourier Transform Infrared Spectroscopy (2nd Ed., CRC Press)

Sree Harsha, K. S. 2005, Principles of Vapor Deposition of Thin Films (Elsevier)

Winn, J. N., Matthews, J. M., Dawson, R. I., et al. 2011, ApJL, 737, L18

APPENDICES

Appendix A. MATLAB Simulation Code

```
% ProgCompare.m
% Denny Bosch, Missouri State University
% Last modified 5/7/2015
%
% Main program script (run this!)
%
% Planet 1 has a CO2 atmosphere. Planet 2 has a SiO atmosphere.
Compare
% the two spectroscopically as seen at various phases.

clear;

% Parameters:
%            T(Star)   T(Plan.)   R(Plan)   R(Star)   R(Orbit)   Albedo
% Earth      5778 K    300 K      6.371e6   6.955e8   1 au       0.3
% 55 CnC e   5373 K    2000 K     1.300e7   8.012e8   0.0156 au  ?
% WASP-12 b  6300 K    2525 K     1.736 RJ  1.599 RS  0.0229 au  ?

AU = 1.496e11;
RE = 6.371e6;
RJ = 6.991e7;
RS = 6.955e8;

starTemp = 6300; % Temperature of the star in Kelvin
planetTemp = 2525; % Temperature of planet's surface in Kelvin
starRadius = 1.599*RS; % Radius of star (must have same units as
planet)
planetRadius = 1.736*RJ; % Radius of planet (must have same units as
star)
orbitalRadius = 0.0229*AU; % Radius of orbit in meters
myphase = 2*pi; % Current orbital phase in radians
inclination = 85.4*pi/180; % Orbital plane's inclination in radians
albedo = 1; % Reflectivity of planet's surface (0-1)



% Create the star's spectrum
% Blackbody radiation (wavenumbers): B(v,T)=2hv^3c^2/(e^hcv/kT-1)

upperBound = 10000; % Spectral range in cm-1
lowerBound = 0;
h = 6.626e-34; c = 3e8; kB = 1.38e-23;
starSpectrumX(upperBound-lowerBound+1) = 0;
starSpectrumY(upperBound-lowerBound+1) = 0;
for x = 1:upperBound-lowerBound+1
    starSpectrumX(x) = x+lowerBound-1;
    starSpectrumY(x) = 2*h*((100*starSpectrumX(x))^3)*(c^2)/...
        exp((h*c*100*starSpectrumX(x)/(kB*starTemp))-1);
end

% Create the absorption spectrum for CO2
```

```
% Place a lorentzian at each peak site with arbitrary intensity and
width
% (temporary)

planet1Peaks = [667 1333 2349];
planet1Absorption(upperBound-lowerBound+1) = 0;
for y = 1:length(planet1Peaks)
    for x = 1:upperBound-lowerBound+1
        FWHM = 20;
        intensity = 10;
        L = FWHM/(2*pi*(x+lowerBound-1-planet1Peaks(y))^2+(FWHM/2)^2);
        if L > 1
            L = 1;
        end
        planet1Absorption(x) = planet1Absorption(x) + L*intensity;
    end
end

% Create the absorption spectrum for SiO2
% Place a lorentzian at each peak site with arbitrary intensity and
width
% (temporary)

planet2Peaks = [767 803 855 945 972 1040 1226];
planet2Absorption(upperBound-lowerBound+1) = 0;
for y = 1:length(planet2Peaks)
    for x = 1:upperBound-lowerBound+1
        FWHM = 20;
        intensity = 10;
        L = FWHM/(2*pi*(x+lowerBound-1-planet2Peaks(y))^2+(FWHM/2)^2);
        if L > 1
            L = 1;
        end
        planet2Absorption(x) = planet2Absorption(x) + L*intensity;
    end
end

% Create planetary spectra

planet1SpectrumY(upperBound-lowerBound+1) = 0;
planet2SpectrumY(upperBound-lowerBound+1) = 0;
planetBlackbody(upperBound-lowerBound+1) = 0;
for x = 1:upperBound-lowerBound+1
    planetBlackbody(x) = 2*h*((100*starSpectrumX(x))^3)*(c^2)/...
        exp((h*c*100*starSpectrumX(x)/(kB*planetTemp))-1);
    planet1SpectrumY(x) = (starSpectrumY(x) + planetBlackbody(x)) * ...
        exp(-planet1Absorption(x));
    planet2SpectrumY(x) = (starSpectrumY(x) + planetBlackbody(x)) * ...
        exp(-planet2Absorption(x));
end

% Create filter spectrum
% Use a clipped gaussian to represent the shape of a filter

filterCenter = 1200;
```

```
filterWidth = 1000;
filterSpectrumY(upperBound-lowerBound+1) = 0;
for x = 1:upperBound-lowerBound+1
    G = 50*exp(-(x+lowerBound-1-filterCenter)^2/(2*(filterWidth/6)^2));
    if G <= 1
        filterSpectrumY(x) = G;
    else
        filterSpectrumY(x) = 1;
    end
end

% Reformat all spectra as two-column XY

for x = 1:length(starSpectrumX)
    starSpectrum(x,1) = starSpectrumX(x);
    starSpectrum(x,2) = starSpectrumY(x);
    planet1Spectrum(x,1) = starSpectrumX(x);
    planet2Spectrum(x,1) = starSpectrumX(x);
    planet1Spectrum(x,2) = planet1SpectrumY(x);
    planet2Spectrum(x,2) = planet2SpectrumY(x);
    filterSpectrum(x,1) = starSpectrumX(x);
    filterSpectrum(x,2) = filterSpectrumY(x);
end

% Quick test calculations

[starFraction, planetFraction] = FracCalc(planetRadius, starRadius, ...
    orbitalRadius, myphase, inclination, albedo);
fullSpectrum1 = SpecGen(planet1Spectrum, starSpectrum, planetFraction,
starFraction);
fullSpectrum2 = SpecGen(planet2Spectrum, starSpectrum, planetFraction,
starFraction);
filteredSpectrum1 = SpecFilter(filterSpectrum, fullSpectrum1);
filteredSpectrum2 = SpecFilter(filterSpectrum, fullSpectrum2);
intensity1 = PhotoOutput(filteredSpectrum1);
intensity2 = PhotoOutput(filteredSpectrum2);

% Quick test output

figure(1);
plot(starSpectrum(:,1),starSpectrum(:,2),starSpectrum(:,1),planetBlackb
ody);
title(['Star Spectrum (T=',num2str(starTemp),')']);
xlabel('wavenumber (cm^{-1})');
figure(2);
plot(planet1Spectrum(:,1),planet1Spectrum(:,2),planet2Spectrum(:,1),pla
net2Spectrum(:,2));
title('Planet Spectra');% (blue=CO2 green=SiO)');
xlabel('wavenumber (cm^{-1})');
figure(3);
plot(filteredSpectrum1(:,1),filteredSpectrum1(:,2),filteredSpectrum2(:,
1),filteredSpectrum2(:,2))
title('Filtered Spectra (blue=CO2 green=SiO)');
xlabel('wavenumber (cm^{-1})');
figure(4);
```

```
plot(filteredSpectrum1(:,1),filteredSpectrum1(:,2)-
filteredSpectrum2(:,2));
title('Difference in Filtered Spectra');
xlabel('wavenumber (cm^{-1})');
ylabel('Intensity normalized to stellar flux');
disp('Calculation complete for one phase! Now running for 100
phases.');
disp(['At phase ',num2str(myphase),', ',num2str(planetFraction/...
    starFraction),' planetary contribution.']);
disp(['CO2: ',num2str(intensity1),', SiO2: ',num2str(intensity2),...
    ', difference: ',num2str(intensity1-intensity2)]);

% Slow test calculations

intensityStar(101)=0;
for t = 1:101
    clear filterSpectrum filteredSpectrum1 filteredSpectrum2

    % Generate new filters
    filterCenters(t) = 490+10*t;
    for x = 1:upperBound-lowerBound+1
        G = 50*exp(-(x+lowerBound-1-
(490+10*t))^2/(2*(filterWidth/6)^2));
        if G <= 1
            filterSpectrum(x,2) = G;
        else
            filterSpectrum(x,2) = 1;
        end
        filterSpectrum(x,1) = starSpectrum(x,1);
    end
    filteredSpectrum1 = SpecFilter(filterSpectrum, fullSpectrum1);
    filteredSpectrum2 = SpecFilter(filterSpectrum, fullSpectrum2);
    filteredStar = SpecFilter(filterSpectrum,starSpectrum);
    intensity1(t) = PhotoOutput(filteredSpectrum1);
    intensity2(t) = PhotoOutput(filteredSpectrum2);
    intensityStar(t) = PhotoOutput(filteredStar);
end

% Slow test output

figure(5);
plot(filterCenters,intensity1,filterCenters,intensity2);
title('Filtered Photometric Intensity (blue=CO2 green=SiO)');
xlabel('Filter center (wavenumber cm^{-1})');
ylabel('Total counts');
figure(6);
plot(filterCenters,intensity1./intensityStar,filterCenters,intensity2./
intensityStar);
title('Filtered Photometric Intensity (blue=CO2 green=SiO)');
xlabel('Filter center (wavenumber cm^{-1})');
ylabel('Relative counts');
figure(7);
plot(filterCenters,intensity1-intensity2);
title('Filtered Photometric Intensity (difference)');
xlabel('Filter center (wavenumber cm^{-1})');
ylabel('Total counts');
```

```
figure(8);
plot(filterCenters,intensity1./intensityStar-
intensity2./intensityStar);
title('Filtered Photometric Intensity (difference)');
xlabel('Filter center (wavenumber cm^{-1})');
ylabel('Relative counts');

% Four photometric points - ratios test

filterBands = [950 2350 4500 9000];
filterWidth = 500;
clear intensity1 intensity2 intensityStar
for t = 1:4
    clear filterSpectrum filteredSpectrum1 filteredSpectrum2

    % Generate new, narrow filters
    for x = 1:upperBound-lowerBound+1
        G = 50*exp(-(x+lowerBound-1-
(filterBands(t)))^2/(2*(filterWidth/6)^2));
        if G <= 1
            filterSpectrum(x,2) = G;
        else
            filterSpectrum(x,2) = 1;
        end
        filterSpectrum(x,1) = starSpectrum(x,1);
    end

    % Calculate photometric intensity
    filteredSpectrum1 = SpecFilter(filterSpectrum, fullSpectrum1);
    filteredSpectrum2 = SpecFilter(filterSpectrum, fullSpectrum2);
    filteredStar = SpecFilter(filterSpectrum,starSpectrum);
    intensity1(t) = PhotoOutput(filteredSpectrum1);
    intensity2(t) = PhotoOutput(filteredSpectrum2);
    intensityStar(t) = PhotoOutput(filteredStar);
end

% Four photometric points - ratios output

figure(9);
plot(filterBands,intensity1,filterBands,intensity2,filterBands,intensit
yStar);
title('Filtered Photometric Intensity (blue=CO2 green=SiO red=none)');
xlabel('Filter center (wavenumber cm^{-1})');
ylabel('Total counts');

disp(['A= ',num2str(filterBands(1)),' cm-1, B=
',num2str(filterBands(2)),...
    ' cm-1, C= ',num2str(filterBands(3)),' cm-1, D=
',num2str(filterBands(4)),' cm-1']);
disp(['No atmosphere: A/B=
',num2str(intensityStar(1)/intensityStar(2)),...
    ', A/C= ',num2str(intensityStar(1)/intensityStar(3)),...
    ', A/D= ',num2str(intensityStar(1)/intensityStar(4))]);
disp(['CO2 atmosphere: A/B= ',num2str(intensity1(1)/intensity1(2)),...
    ', A/C= ',num2str(intensity1(1)/intensity1(3)),...
```

```
    ', A/D= ',num2str(intensity1(1)/intensity1(4))]);
disp(['SiO atmosphere: A/B= ',num2str(intensity2(1)/intensity2(2)),...
    ', A/C= ',num2str(intensity2(1)/intensity2(3)),...
    ', A/D= ',num2str(intensity2(1)/intensity2(4))]);

disp('Done!');

break;
```

```
% FracCalc.m
% Denny Bosch, Missouri State University
% Last modified 1/16/2013
%
% Calculate the fraction of original intensity containing absorbance
peaks
% and the fraction containing just starlight

function [starFrac, planetFrac] = FracCalc(radPlanet, radStar,
radOrbit,...
    phase, inclination, albedo)
% inclination = [0,pi/2] angle with respect to the viewing plane
% phase = [0,2pi] in-plane angle of orbit

% Initialization
planetFrac = 0;
starFrac = 1;

alpha = real(atan(radStar/sqrt(radOrbit^2-radStar^2))); % 1/2 transit
angular size (re: phase)
beta = 2*real(atan(radPlanet/radOrbit)); % planet angular size (re:
phase)

% Proportion of light absorbed by the planet depends on visible
% illuminated area and planet:star size ratio
absorbed = 0.5*(1-cos(phase+pi/2))*(radPlanet/radStar)^2 /
(radOrbit/radStar)^2;%*(radPlanet/radOrbit)^2;
% Of that proportion, a fraction depending on orbital distance and
albedo
% is reflected:
 reflectFrac = absorbed * albedo;% / (4*pi*radOrbit);
%reflectFrac = absorbed * albedo / radOrbit/radStar;

% CASE 1: Planet hidden behind star
if phase > (pi/2)-alpha && phase < (pi/2)+alpha
    % CASE 1A: Planet fully obscured
    if phase > (pi/2)-alpha+beta && phase < (pi/2)+alpha-beta
        % No contribution from planet, full contribution from star
        planetFrac = 0;
        starFrac = 1;
    % CASE 1B: Planet partially obscured
    else
        % Stellar contribution is unchanged
        starFrac = 1;
        % Calculate area of planet obscured
        x = (phase - pi/2)*(radStar/alpha);
        y = x * atan(inclination);
        d = sqrt(x^2+y^2);
        A = real(radPlanet^2 * acos((d^2 + radPlanet^2 - radStar^2)/
...
            (2*d*radPlanet)) + radStar^2 * acos((d^2 + radStar^2 -
...
            radPlanet^2)/(2*d*radStar))-0.5*sqrt((-d+radPlanet+radStar)
...
            *(d+radPlanet-radStar)*(d-radPlanet+radStar)*
...
```

```
            (d+radPlanet+radStar))); % Area of intersection of 2
circles
        % Reflected fraction is reduced by area of intersection
        planetFrac = reflectFrac * (pi*radPlanet^2 -
A)/(pi*radPlanet^2);
    end
% CASE 2: Planet transiting in front of star
elseif phase > (3*pi/2)-alpha && phase < (3*pi/2)+alpha
    % Atmospheric illumination area is given by mass and temperature:
    temperature = 1000; % Need the planet's temperature (get this as
input?)
    molecularWeight = 28.97*6.022e23; surfaceGravity = 9.8;% = ?
    kT = 1.3806488e-23 * temperature;
    H = kT / (molecularWeight*surfaceGravity) ;
    % CASE 2A: Full occultation (entirety of planet over star)
    if phase > (3*pi/2)-alpha+beta && phase < (3*pi/2)-beta
        % Planet obscures a portion of the star's surface
        starFrac = 1 - (radPlanet/radStar)^2;
        % Planet's atmosphere adds an annular transmission component
        atmosphere = pi*radPlanet^2-pi*(radPlanet-5*H)^2;
        %atmosphere = 0; % NO CONTRIBUTION
        planetFrac = atmosphere/(pi*radStar^2) + reflectFrac;
    % CASE 2B: Partial occultation (part of planet is not covering
star)
    else
        % Calculate the areas of intersection
        x = (phase - 3*pi/2)*(radStar/alpha);
        y = x * atan(inclination);
        d = sqrt(x^2+y^2);
        A = real(radPlanet^2 * acos((d^2 + radPlanet^2 - radStar^2)/
...
            (2*d*radPlanet)) + radStar^2 * acos((d^2 + radStar^2 -
...
            radPlanet^2)/(2*d*radStar))-0.5*sqrt((-d+radPlanet+radStar)
...
            *(d+radPlanet-radStar)*(d-radPlanet+radStar)*
...
            (d+radPlanet+radStar))); % Area of intersection of 2
circles
        % Planet obscures intersectional area
        starFrac = 1 - A/(pi*radStar^2);
        % Calculate the area of intersection with atmospheric annulus
        innerA = real((radPlanet-5*H)^2 * acos((d^2 + (radPlanet-5*H)^2
...
            - radStar^2)/ (2*d*(radPlanet-5*H))) + radStar^2 *acos((d^2
...
            + radStar^2 - (radPlanet-5*H)^2)/(2*d*radStar))-0.5*sqrt((-
d...
            +(radPlanet-5*H)+radStar) *(d+(radPlanet-5*H)-radStar)*(d-(
...
            radPlanet-5*H)+radStar)* (d+(radPlanet-5*H)+radStar)));
        atmosphere = A - innerA;
        %atmosphere = 0; % NO CONTRIBUTION
        planetFrac = atmosphere/(pi*radStar^2) + reflectFrac;
    end
% CASE 3: No transit, planet to the side of star
else
```

```
    % No obscuration of starlight
    starFrac = 1;
    % Planetary emission component
    planetFrac = reflectFrac;
end

% Output absorbance fraction
[starFrac, planetFrac];
```

```
% SpecGen.m
% Denny Bosch, Missouri State University
% Last modified 1/16/2013
%
% Generate stellar spectrum containing planetary transit from
unmodified
% spectrum from database and absorbance spectrum from program

function spectrum = SpecGen(varargin)

% Initialization
spectrum = [0,0];
absoSpec = [0,0];
starSpec = [0,0];
absoFrac = 0;
starFrac = 1;

if nargin == 0 % No input arguments
    % Ask user for absorbance spectrum file position
    filename = uigetfile('*.csv',
...
        'Select the absorbance spectrum file to be processed');
    % Get absorbance spectrum from CSV
    absoSpec = csvread(filename);
    % Ask user for star spectrum file position
    filename = uigetfile('*.csv',
...
        'Select the stellar spectrum file to be processed');
    % Get star spectrum from CSV
    starSpec = csvread(filename);
    % Get absorbance fraction from user
    absoFrac = inputdlg('Enter fraction of light affected by
atmosphere');
    starFrac = inputdlg('Enter fraction of unaltered starlight');
elseif nargin == 4 % Absorbance spectrum, star spectrum, and fractions
    if size(varargin{1}) > [1,0]
        absoSpec = varargin{1};
    else
        absoSpec = csvread(varargin{1});
    end
    if size(varargin{2}) > [1,0]
        starSpec = varargin{2};
    else
        starSpec = csvread(varargin{2});
    end
    absoFrac = varargin{3};
    starFrac = varargin{4};
else % Wrong number of arguments
    error(strcat('Bad input. Try SpecGen(''filename1'', ''filen', ...
        'ame2'', frac1, frac2) or SpecGen(matrix1, matrix2, n1,
n2).'));
end

% Subtract absorbance spectrum weighted at absorbance fraction
for index = 1:length(starSpec(:,1))
    spectrum(index,1) = starSpec(index,1);
```

```
    if index <=length(absoSpec(:,1))
        spectrum(index,2) = starSpec(index,2) *        ...
        starFrac - absoSpec(index,2) * absoFrac;
    else
        spectrum(index,2) = starSpec(index,2);
    end
end

% Output complete spectrum
spectrum;
```

```
% SpecFilter.m
% Denny Bosch, Missouri State University
% Last modified 12/19/2013
%
% Convolve spectrum with filter transmittance from database

function spectrum = SpecFilter(varargin)

% Initialization
starSpec = [0,0];
filtSpec = [0,0];
spectrum = [0,0];

if nargin == 0 % No arguments passed
    % Ask user for spectrum file position
    filename = uigetfile('*.csv',
...
        'Select the spectrum file to be processed');
    % Get spectrum from CSV
    starSpec = csvread(filename);
    % Ask user for filter file position
    filename = uigetfile('*.csv',
...
        'Select the filter file to be processed');
    % Get filter transmittance from CSV
    filtSpec = csvread(filename);
end

if nargin == 1 % Only spectrum passed
    if size(varargin{1}) > [1,0]
        starSpec = varargin{1};
    else
        starSpec = csvread(varargin{1});
    end
    % Ask user for filter file position
    filename = uigetfile('*.csv',
...
        'Select the filter file to be processed');
    % Get filter transmittance from CSV
    filtSpec = csvread(filename);
end

if nargin == 2 % Spectrum and filter passed
    if size(varargin{1}) > [1,0]
        starSpec = varargin{1};
    else
        starSpec = csvread(varargin{1});
    end
    if size(varargin{2}) > [1,0]
        filtSpec = varargin{2};
    else
        filtSpec = csvread(varargin{2});
    end
end

if nargin > 2 % Too many arguments
```

```
    error(strcat('Too many inputs. Try SpecFilter(''filename1'', ''fi',
...
        'lename2'') or SpecFilter(matrix1, matrix2).'));
end

% Determine filter offset (if any)
[shift,junk] = find(filtSpec == starSpec(1,1)); clear junk;
shift = shift(1)-1;
% Multiply spectrum by transmittance percentage
for index = 1:length(filtSpec(:,1))-shift
    spectrum(index,1) = filtSpec(index,1);
    spectrum(index,2) = starSpec(index+shift,2) * filtSpec(index,2);
end

% Output convolved spectrum
spectrum;
```

```
% PhotoOutput.m
% Denny Bosch, Missouri State University
% Last modified 12/19/2013
%
% Calculate photometer output (single point intensity) for a given
spectrum

function intensity = PhotoOutput(varargin)

% Initialization
intensity = 0;
spectrum = [0,0];

if nargin == 0 % No arguments passed
    % Ask user for spectrum file position
    filename = uigetfile('*.csv',
...
        'Select the spectrum file to be processed');
    % Get spectrum from CSV
    spectrum = csvread(filename);
end

if nargin == 1 % Spectrum file path or complete spectrum passed
    if size(varargin{1}) > [1,0]
        spectrum = varargin{1};
    else
        spectrum = csvread(varargin{1}); % Get spectrum from CSV
    end
end

if nargin > 1 % Too many arguments
    error(strcat('Too many inputs. Try PhotoOutput(''filename'') or P',
...
        'hotoOutput(matrix).'));
end

% Integrate over all wavelengths
for index = 1:length(spectrum)
    intensity = intensity + spectrum(index,2);
end

% Output intensity value
intensity;
```

Appendix B. MATLAB Spectral Analysis Code

```
% Denny Bosch 9/9/2013 - 6/10/2015
clear; clc;

pow = 3; % Polynomial fit order
tol = 0.5; % reject data outside of (tol*sigma) deviation as non
background

%% File input
fprintf('Select the Background File:\t');
[file,path] = uigetfile('*.csv','Select the Background File',...
    'C:\My Documents\OMNIC\Spectra\DennyCurtisNolan\2 hrs SiO2 @1600C,
Wed Apr 29 15-46-09 2015 (GMT-05-00) CUTS');
bkgdata = csvread(strcat(path,file));
fprintf(strcat(file,' OK.\nSelect the Sample File:\t'));
[file,path] = uigetfile('*.csv','Select the Sample File',...
    'C:\My Documents\OMNIC\Spectra\DennyCurtisNolan\2 hrs SiO2 @1600C,
Wed Apr 29 15-46-09 2015 (GMT-05-00) CUTS');
smpdata = csvread(strcat(path,file));
fprintf(strcat(file,' OK.\nCalculating... '));
[bkgmin,mindex] = min(bkgdata(:,2));

%% Calculation
len = length(bkgdata(:,1)); % Preallocate arrays
data(len,2) = 0; lindata(len) = 0; polydata(len,1) = 0;
for n = 1:len % Log division
    data(n,1) = bkgdata(n,1);
    data(n,2) = -
log(smpdata(n,2)*bkgmin/(smpdata(mindex,2)*bkgdata(n,2)));
end
for n = 1:len % Simple linear fitting from endpoints
    lindata(n) = data(n,2) - data(1,2) - (data(len,2) -
data(1,2))*(data(n,1) - data(1,1))/(data(len,1) - data(1,1));
end
sd = std2(lindata); m = 0; % Separate non-peak data (linbg)
for n = 1:len
    if abs(lindata(n)) < sd*tol
        m = m + 1;
        linbg(m,1) = data(n,1);
        linbg(m,2) = lindata(n);
    end
end
p = polyfit(linbg(:,1),linbg(:,2),pow); % Polynomial fitting of order
pow
polybg = polyval(p,data(:,1));
for n = 1:len
    polydata(n,1) = lindata(n) - polybg(n); % Subtract polynomial
background from data
end

%% Integration (Rheimann Sum)
dx = data(2,1)-data(1,1);
rsum = 0;
for n = 1:len
```

```
    rsum = rsum + polydata(n,1)*dx;
end
rsum

%% Output
plot(bkgdata(:,1),bkgdata(:,2),smpdata(:,1),smpdata(:,2),...
    data(:,1),polydata(:,1));
set(gca,'XDir','reverse');
pause(0.1);
fprintf(' completed without errors.\nSave result as CSV: ');
[file,path] = uiputfile('*.csv','Save result as CSV',...
    'C:\My Documents\OMNIC\Spectra\DennyCurtisNolan\2 hrs SiO2 @1600C,
Wed Apr 29 15-46-09 2015 (GMT-05-00) CUTS');
csvwrite(strcat(path,file),[data(:,1),polydata(:,1)]);
fprintf(strcat(file,' OK.\n\nDone. :)\n'));
```

Appendix C. Additional Research

Over the course of this research project, a number of avenues were considered and attempted with varying degrees of success. The route which was ultimately pursued after proving the most successful was detailed in the engineering section of this thesis. A brief sampling of alternative processes which did not pan out are provided here for the benefit of the reader.

Originally, this project was meant to be carried out using an EFM 3 evaporator. However, it was discovered the hard way that the EFM 3 was limited in its temperature range and prone to malfunctions: short-circuits, filament burnout, contamination issues, etc; all of which required exhaustive maintenance. The EFM 3 was also highly unstable, requiring constant supervision and adjustment to provide a constant rate of flux, and both of its power supplies ultimately failed. While preliminary experiments were conducted using the EFM 3, an effort was made to locate a commercial alternative. Ultimately, although a number of manufacturers provided quotes for potential alternative systems, the decision was made to build an in-house system which would be cheaper, easier to maintain, and tailored to the needs of the project.

Early efforts to make measurements of high temperature vapors were frustrated by an inability to achieve the desired temperatures and deposition rates. Initially, open crucibles purchased from the evaporator supplier were used, but these deposited many orders of magnitude more flux than was desired and were not representative of equilibrium conditions. A basic Knudsen cell crucible design was manufactured by the machinist at Missouri State, using materials on hand; this crucible was a precursor to the design pictured in the engineering section of this thesis. The biggest flaw with this crucible was its mass, several grams greater than that of the previously used crucibles. The larger crucible could only achieve temperatures several hundred degrees below that of the original crucibles. This led to a creative reduction of mass while retaining the interior volume by our machinist, resulting in the final design described after several attempts. It also caused the crucibles to become brittle, and several cracked after repeated use.

A number of decisions were made during the design of the evaporator which were proven to be flawed during the initial testing process and which did not appear in the final design. A prominent example of this is the basic structure of the first evaporator constructed: instead of the molybdenum scaffolding and feedthrough pins described in this thesis, it used 1mm threaded rods to hold the filament loop. It soon became apparent that the rods were prone to moving independently of one another, and even the slightest vibration was magnified by the length of the rods, so machinable ceramic parts were made to dampen vibrations – with the caveat that machinable ceramic cannot withstand the high temperatures the evaporator would subject it to. In addition, the thick rods acted as a heat sink, making heating the filament between them (which had a much smaller

mass) extremely difficult. This led to the use of feedthrough pins, which allowed for a metal structure instead of machinable ceramic, using high temperature ceramic for insulation.